

# **MicroBooNE: Neutron Induced Cosmogenic $\pi^0$ s**

**Ryan A. Grosso**

Submitted in partial fulfillment of the  
requirements for the degree  
of Doctor of Philosophy  
in the Graduate School of Arts and Sciences

**UNIVERSITY OF CINCINNATI**

2018

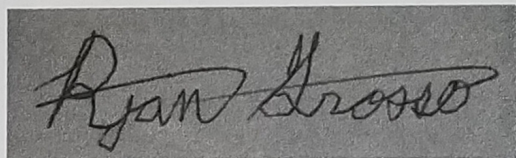
©2018

Ryan A. Grosso

All Rights Reserved

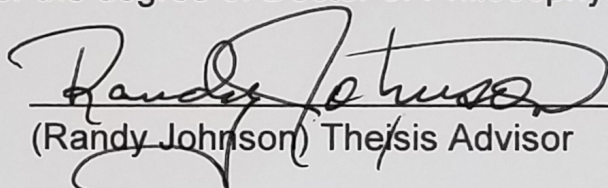
University of Cincinnati

Department of Physics of the College of Arts and Science



(Ryan Grosso)

I certify that I have read this dissertation and that, in my opinion, it is fully adequate in scope and quality as a dissertation for the degree of Doctor of Philosophy.



---

(Randy Johnson) Thesis Advisor

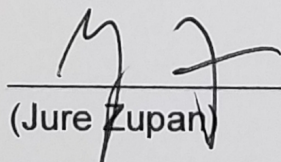
I certify that I have read this dissertation and that, in my opinion, it is fully adequate in scope and quality as a dissertation for the degree of Doctor of Philosophy.



---

(Alexandre Sousa)

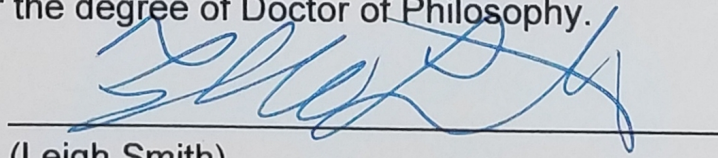
I certify that I have read this dissertation and that, in my opinion, it is fully adequate in scope and quality as a dissertation for the degree of Doctor of Philosophy.



---

(Jure Zupan)

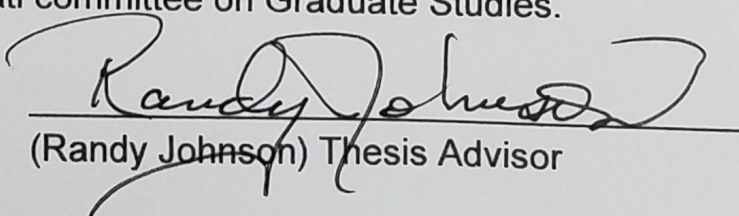
I certify that I have read this dissertation and that, in my opinion, it is fully adequate in scope and quality as a dissertation for the degree of Doctor of Philosophy.



---

(Leigh Smith)

Approved for the University of Cincinnati committee on Graduate Studies.



---

(Randy Johnson) Thesis Advisor

*Thanks Mom and Dad.*

*This is for you!*

# Table of Contents

<b>List of Figures</b>	iii
<b>List of Tables</b>	v
<b>1 Introduction</b>	1
<b>2 Neutrinos &amp; Neutrino Oscillations</b>	3
2.1 The History the Neutrino . . . . .	3
2.2 Discovery of the Neutrino . . . . .	5
2.3 Neutrinos in the Standard Model . . . . .	8
2.4 Neutrino Interactions . . . . .	9
2.5 Neutrino Mass and Flavor Oscillations . . . . .	12
2.6 Sterile Neutrinos . . . . .	17
<b>3 The MicroBooNE Detector</b>	19
3.1 Brief History of LAr-TPCs . . . . .	19
3.2 Introduction . . . . .	20
3.3 Time Projection Chamber . . . . .	21
3.4 Light Collection . . . . .	27
3.5 Electronics Readout . . . . .	29
<b>4 Booster Neutrino Beam</b>	32
4.1 Primary Beam, Target and Horn . . . . .	33
4.2 Neutrino Flux Prediction . . . . .	34

<b>5 Low Energy Excess and Relevant Cross Sections</b>	<b>37</b>
5.1 Overview . . . . .	37
5.2 LSND Excess . . . . .	37
5.3 MiniBooNE Excess . . . . .	39
5.4 Neutral Current $\pi^0$ Production . . . . .	40
5.5 NC- $\pi^0$ in Carbon vs Argon . . . . .	42
<b>6 Cosmogenic <math>\pi^0</math>s at MicroBooNE</b>	<b>43</b>
6.1 Motivation . . . . .	43
6.2 Traditional Reconstruction . . . . .	45
6.3 Wire Cell Imaging . . . . .	46
6.4 Pattern Recognition . . . . .	47
6.5 Clustering . . . . .	48
6.6 Track and Shower Selection . . . . .	50
6.6.1 Track Removal . . . . .	50
6.6.2 Single $\pi^0$ Reconstruction . . . . .	50
6.7 Single $\pi^0$ Cosmic Sample . . . . .	54
<b>7 Results</b>	<b>58</b>
7.1 Monte Carlo Simulation . . . . .	58
7.2 Data . . . . .	61
7.3 Data-Monte Carlo Comparison . . . . .	61
<b>8 Conclusions</b>	<b>64</b>
8.1 Conclusion . . . . .	64
<b>I Appendices</b>	<b>65</b>
<b>Bibliography</b>	<b>68</b>

# List of Figures

2.1	Cowan and Reines first proposed neutrino experiment. . . . .	5
2.2	The hadron production cross section around the $Z^0$ resonance from LEP. . . . .	7
2.3	The Standard Model . . . . .	9
2.4	Charge and Neutral Current Interactions . . . . .	12
2.5	This plot shows the appearance and disappearance curves for a 2-flavor approximation as a function of baseline. The values of $\Delta m^2 = 0.0025 \text{ eV}^2$ and $\sin^2 \theta = 0.14$ are used. . . . .	14
2.6	Neutrino Mass Hierarchy . . . . .	16
2.7	Sterile Neutrinos . . . . .	18
3.1	Diagram of a Time Projection Chamber . . . . .	20
3.2	MicroBooNE TPC . . . . .	22
3.3	MicroBooNE wires measured linear mass density . . . . .	23
3.4	Tensioning system . . . . .	24
3.5	Multiple wire planes installed in MicroBooNE . . . . .	25
3.6	MicroBooNE tension measuring device . . . . .	26
3.7	MicroBooNE tension map . . . . .	27
3.8	MicroBooNE tension histogram . . . . .	27
3.9	PMT optical unit . . . . .	28
3.10	PMT optical unit . . . . .	29
3.11	Detector Electronic layout . . . . .	30
4.1	The Booster Neutrino Campus . . . . .	32

4.2	BNB Target . . . . .	34
4.3	Booster Neutrino Beamline . . . . .	35
4.4	BNB Target . . . . .	36
5.1	LSND Excess . . . . .	38
5.2	MiniBooNE Event topology . . . . .	40
5.3	MiniBooNE excess for $\nu$ and $\bar{\nu}$ . . . . .	41
5.4	Neutrino induces single $\pi^0$ production . . . . .	42
6.1	Icarus Cosmic $\pi^0$ . . . . .	45
6.2	Wire Cell reconstruction of CORSIKA MC viewed in the BEE viewer . . . . .	48
6.3	Images from the BEE-WireCell image viewer. . . . .	49
6.4	Photon distribution from $\pi^0$ s . . . . .	51
6.5	Reconstructed energy sum and energy product for shower pairs. Both, the reconstructed energy sum and product is less than the true energy deposited.	52
6.6	Reconstructed vs. True opening angle . . . . .	53
6.7	Single particle $\pi^0$ mass distribution . . . . .	54
6.8	Single particle $\pi^0$ reconstruction efficiency . . . . .	55
6.9	Cosmic $\pi^0$ production by parent process . . . . .	56
6.10	Spatial decay points for cosmic $\pi^0$ s in MicroBooNE . . . . .	57
7.1	Enhanced Signal Sample . . . . .	60
7.2	Background Sample . . . . .	61
7.3	Area normalized Data-Monte Carlo mass distributions . . . . .	62
7.4	Direct data Monte Carlo rate comparison . . . . .	63
7.5	Direct data Monte Carlo rate comparison . . . . .	63

# List of Tables

4.1 Beam Production Systematics . . . . .	36
7.1 CORSIKA MC rates . . . . .	59

# Chapter 1

## Introduction

This thesis describes work towards electromagnetic shower reconstruction and steps towards a neutral current single  $\pi^0$  cross section measurement motivated from reconstruction techniques used for neutron induced cosmogenic  $\pi^0$  analysis. This thesis will use data from the MicroBooNE Liquid Argon Time Projection Chamber (LArTPC) located at the Fermi National Accelerator in Batavia, IL.

To begin, Chapter 2 will provide some background about the neutrino. We will begin by presenting the initial premise for the need of a neutrino-like particle. Then, we will describe the theoretical framework used to address how they interact the standard model. Finally we will present the phenomenon known as neutrino oscillation and provide some mathematical framework to describe it. Chapter 3 begins with a brief history of the LArTPC detector technology and its use as a high precision neutrino detector. The chapter continues to explain in depth the various subsystems that constitute the MicroBooNE detector. Chapter 4 will describe how a neutrino beam is produced and delivered to the MicroBooNE detector. It will focus on Fermilab's Booster Neutrino Beam (BNB) which generates a beam of nearly pure  $\nu_\mu$  or  $\bar{\nu}_\mu$  around 1 GeV in average energy. Chapter 5 will present in detail the claims of the electromagnetic  $\nu_e$ -like excess first seen by the LSND experiment and then later verified by the MiniBooNE experiment. This chapter will also discuss the neutral current cross section, which is the main background in the MiniBooNE excess claim. Chapter 6 will introduce MicroBooNE's cosmogenic background and motivate the importance of

understanding the cosmic rate. Here, we will also discuss the motivation to use cosmic  $\pi^0$  events as a means of calibrating the detector energy scale. The cosmic backgrounds are addressed for the oscillation analysis and a future neutral current single  $\pi^0$  measurement. Next, this chapter will address simulation, reconstruction, and event selection. Chapter 7 will present results from MicroBooNE cosmics data addressing the cosmic  $\pi^0$  rate from neutral induced events. We will finish with conclusions from both the measurement and also comments on a new technique towards EM reconstructed showers.

## Chapter 2

# Neutrinos & Neutrino Oscillations

### 2.1 The History the Neutrino

The story of the neutrino began in Paris on a cloudy winter day in the year 1896. Parisian native, Henri Becquerel was experimenting with Uranium salts and investigating the newly discovered x-ray radiation. [1] He hypothesized that when the salts were energized by sunlight they would produce the x-ray radiation. This hypothesis was disproven on the cloudy February 27th day when his experiment still detected radiation emitting from the salts in the absence of the sun. Becquerel had discovered radioactivity. In the coming years, this phenomena was supported by the work of Marie and Pierre Curie in studying the radioactivity of the element Thorium which lead to their discovery of the elements Polonium and Radium. These discoveries would later win Becquerel and the Curie's the 1903 Nobel Prize in Physics.

After radioactivity became an accepted phenomena in the science community, Ernst Rutherford discovered that radioactive decay products came in two different forms. He labeled them as  $\alpha$ -decay and  $\beta$ -decay. At the time, beta decay was believed to be a two body decay where a nucleus  $A$  decays into a lighter nucleus  $A'$  and a  $\beta$ -particle(electron). The outgoing energy of the electron from a two body decay is given by equation 2.1. Assuming conservation of energy, the value of the outgoing energy should be discrete.

$$E_e = \frac{m_A^2 + me^2 - m_{A'}^2}{2m_A} \quad (2.1)$$

In 1914, James Chadwick had discovered that the energy spectrum of the  $\beta$ -particles were continuous as opposed to mono-energetic. While some scientist were willing to abandon the requirement of energy conservation, others found this to be an unpalatable solution. Unable to attend the 1930 Tubingen physics conference in Germany, Wolfgang Pauli wrote a letter to the attendees in which he proposed the first idea of the neutrino. An excerpt from his famous December 4th letter is translated from German below [2].

I have hit upon a desperate remedy to save the “exchange theorem” of statistics and the law of conservation of energy. Namely, the possibility that there could exist in the nuclei electrically neutral particles, that I wish to call neutrons, which have spin 1/2 and obey the exclusion principle and which further differ from light quanta in that they do not travel with the velocity of light. The mass of the neutrons should be of the same order of magnitude as the electron mass and in any event not larger than 0.01 proton masses. The continuous beta spectrum would then become understandable by the assumption that in beta decay a neutron is emitted in addition to the electron such that the sum of the energies of the neutron and the electron is constant...

In 1932, Chadwick discovered the neutron we know of today. Unfortunately, this neutron was too heavy to be the particle that Pauli had proposed. Expanding on Pauli’s work, Enrico Fermi proposed a more complete picture of beta decay and renamed Pauli’s ‘neutron’ to what is commonly called a *neutrino*. Fermi’s theory directly coupled the neutron with a final state proton, electron, and neutrino. This theory of beta decay,  $n \rightarrow p + e^- + \bar{\nu}_e$  preserves the law of conservation of energy and would later prove to be a more accurate description of the process.

## 2.2 Discovery of the Neutrino

Measuring and detecting neutrinos is a tricky business. In the 1950s, Clyde Cowan and Frederick Reines set out to directly measure neutrino interactions for the first time. If a free neutrino existed, they hypothesized that they could detect the byproducts from the inverse beta decay  $\bar{\nu}_e + p \rightarrow e^+ + n$ . They realized that such a measurement would require a very intense neutrino source and a large detector. Their first proposal, which was approved, was to detonate a nuclear bomb to supply the large, instantaneous source of neutrinos. A large detector filled with liquid scintillator would free fall down a mine shaft recording flashes of light from the ionizing positrons before landing on a bed of feathers and foam rubber. The original experimental schematic is shown in Figure 2.1. At that time, the theorized neutrino cross section was  $10^{-43} \text{ cm}^2/\text{proton}$  while the existing measured limit was still 7 orders of magnitude short in sensitivity. The bomb experiment would have worked but could not provide the level of sensitivity required to confirm detection for neutrino cross sections below  $10^{-39} \text{ cm}^2/\text{proton}$ . This was due to background interactions that came in time directly from the bomb.

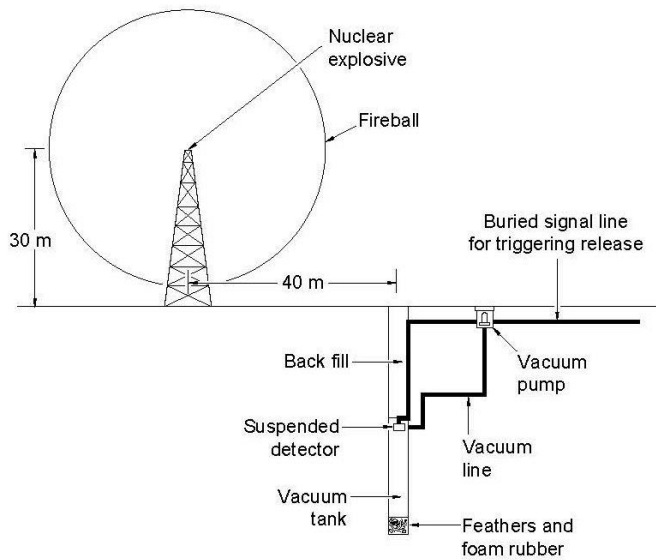
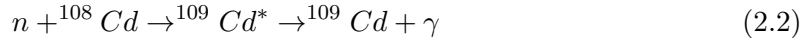


Figure 2.1: Original sketch of Cowan and Reines first proposed neutrino experiment.

Later, Reines realized tagging both the positron and neutron through a double coincidence would drastically reduce the backgrounds. This meant they could use a less intense neutrino source such as a nuclear reactor. They chose the Savannah River Plant near Augusta, Georgia which was estimated to produce neutrino fluxes on the order of  $10^{12} - 10^{13}$  neutrinos/s/cm<sup>2</sup>. The detector was composed of a water target that was doped with CdCl<sub>2</sub>. As stated prior, the signal would rely on a double coincidence flash measured from photomultiplier tubes inside their detector. First, they would detect the positron as it annihilates with an electron via pair production ( $e^+ + e^- \rightarrow \gamma + \gamma$ ). This is identified by two, back-to-back, coincident 0.511 MeV photons. Then, approximately 5  $\mu$ s later, a secondary photon would be detected which was produced from the neutron capture on Cadmium as shown in equation 2.2.



In 1956, only 25 years after Pauli's initial proposal of the neutrino, Cowan and Reines succeeded and provided the first direct experimental evidence of the electron flavor neutrino. In the subsequent years, the existence of two other flavors of neutrinos have been verified. In 1962, Lederman, Schwartz, and Steinberger discovered the  $\nu_\mu$  at Brookhaven National Laboratory by measuring neutrinos coming from pion decay. The  $\nu_\mu$  would be distinctly different from that of  $\nu_e$  if the process  $\nu_\mu + n \rightarrow p + e^-$  was forbidden. The results showed that the neutrinos from pion decay were indeed muon-like. Finally in 2000, the DONUT (Direct Observation of NeUtrino Tau) experiment stationed at Fermilab, made the first observed measurement of the  $\nu_\tau$ .

In 1956, C.S. Wu had shown that outgoing electron from beta decay maintained an opposing spin with respect to the spin of the parent nucleus. This turned out to be the first proof of maximal parity violation in weak interactions. Shortly thereafter, the neutrino helicity was first measured at Brookhaven National Labs by Maurice Goldhaber. In nature, neutrinos only have left handed helicity, while anti-neutrinos have right handed helicity. Helicity is frame dependent for particles with mass, which means there can be a reference frame in which the momentum vector can switch but the spin vector will not. For a

mass zero particles, this is not possible because the particle would already be traveling at the speed of light. This assumption is what led to the belief that neutrinos were massless.

The number of active light neutrinos is well constrained by studying the decay of the  $Z^0$  boson at LEP (Large Electron-Positron collider). LEP was an electron-positron collider ring with a circumference of approximately 27 km that supported four primary experiments (L3, ALEPH, OPAL and DELPHI). The facility was coined the phrase “Z-Factory” due to its ability to record approximately 1000  $Z^0$  boson decays every hour during optimal running conditions. The number of active neutrinos,  $N_\nu$ , is related to the width of the  $Z^0$  resonance. Using 17 million  $Z^0$  decays, LEP was able to show that  $N_\nu = 2.9840 \pm 0.0082$

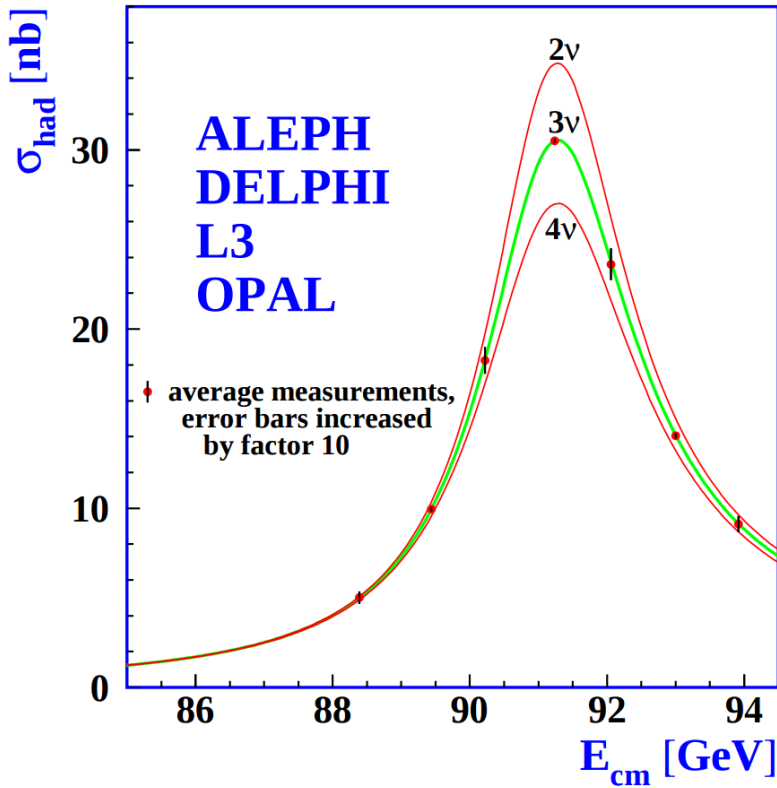


Figure 2.2: The Hadron production cross section around the  $Z^0$  resonance from LEP. The curves for two, three, and four neutrino flavors are shown. The fit shows very compelling evidence of three active flavors of neutrinos.

## 2.3 Neutrinos in the Standard Model

In the later half of the 20th century, scientists were looking for a way to describe all the fundamental forces and classify the known particles. The standard model of particle physics is a phenomenological framework that describes the interaction of fundamental particles between the strong and electroweak forces. Having stood the test of time, the standard model accurately predicts most elementary particle interactions, but, does have its limitations. The standard model does not account for gravity nor does it account for many new physics phenomena such as dark matter or dark energy. Most importantly, as we will see in section 2.5, it does not provide an accurate description of the neutrino.

The standard model consists of two types of particles, bosons and fermions. The fundamental bosons consist of two families: gauge bosons, which are typically the force carriers, and scalar bosons, which refer to spin zero particles or fields. The gluon, photon, and the weak boson are gauge bosons that mediate the strong, electromagnetic, and weak forces, respectively. The Higgs boson is a scalar boson that possesses a nonzero vacuum expectation value of 246 GeV. This provides a mechanism for certain particles to gain mass even though their symmetries would suggest zero mass. The fundamental fermions are also divided into two families, quarks and leptons each having three generations. The quarks compose two main categories of particles, baryons and mesons. Baryons consist of an ensemble of 3 quarks. The most common and stable baryons in the universe are protons ( $uud$ ) and neutrons ( $udd$ ). Meson consist of an ensemble of quark anti-quark pairs and tend to have shorter lifetimes than their corresponding baryons. The lightest and most common mesons are pions ( $u\bar{d}, d\bar{u}, u\bar{u}/d\bar{d}$ ) and kaons ( $u\bar{s}, s\bar{u}, d\bar{s}/s\bar{d}$ ). The leptons are also divided into two families with three generations each. The charged leptons, most notably the electron, interact via the electromagnetic and weak nuclear force and combine with nuclei to form stable baryonic matter. The neutral leptons are the neutrinos and only interact via the weak nuclear force. More details such as mass, charge, and spin for various particles are shown in figure 2.3

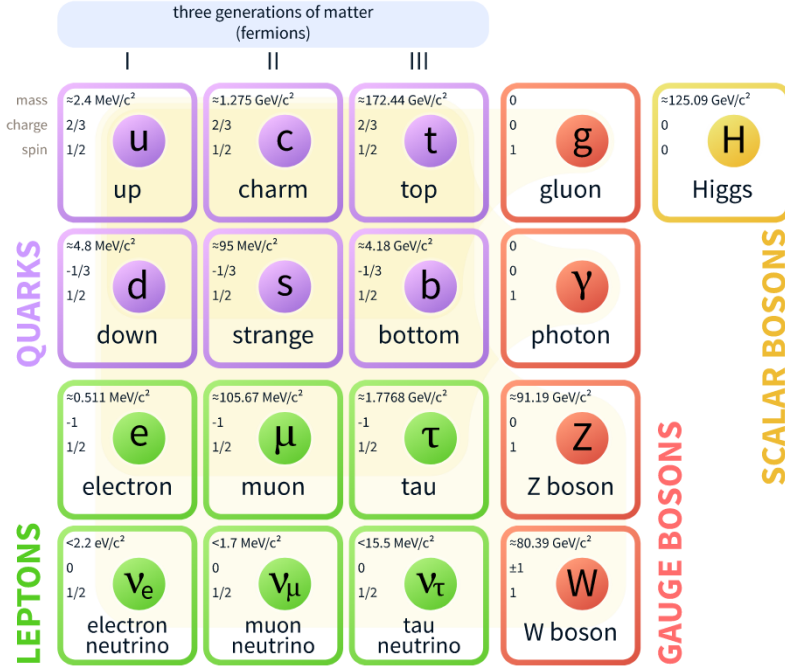


Figure 2.3: The current view of the standard model.

## 2.4 Neutrino Interactions

Neutrinos interact via the weak force. In the standard model, the weak force is unified with the electromagnetic force through an  $SU(2) \otimes U(1)$  symmetry. The structure of the  $SU(2)$  group symmetry accounts for the chirality of the fermion fields, along with ability to produce massive gauge bosons. The  $U(1)$  group symmetry accounts for the massless photon propagator needed for electromagnetic interactions. For the quark and fermion families we define fermion fields in equations 2.3 and 2.4 , respectively. For formality we will define right(left)- handed neutrino(anti-neutrino) fields knowing that they will become irrelevant as the theory evolves:

$$\psi_1(x) = \begin{pmatrix} q \\ q' \end{pmatrix}_L , \quad \psi_2 = q_R , \quad \psi_3 = q'_R \quad (2.3)$$

$$\psi_1(x) = \begin{pmatrix} \nu \\ l \end{pmatrix}_L , \quad \psi_2 = \nu_R , \quad \psi_3 = l_R \quad (2.4)$$

We begin with the free Lagrangian, defined in equation 2.5, as it is already invariant in flavor space.

$$\mathcal{L}_{\text{free}} \equiv \bar{\psi}(i\cancel{\partial} - m)\psi = i\bar{\psi}(x)\gamma^\mu\partial_\mu\psi(x) - m\bar{\psi}(x)\psi(x) \quad (2.5)$$

To make the Lagrangian invariant under local  $SU(2) \otimes U(1)$ , the fermion derivatives have to be changed to covariant objects. This produces 4 different gauge parameters, shown in equations 2.6, which correspond to the 4 different gauge fields required to describe the  $W^\pm$ ,  $Z^0$ , and  $\gamma$ .

$$\begin{aligned} D_\mu\psi_1(x) &\equiv [\partial_\mu - ig\widetilde{W}_\mu(x) - ig'y_1B_\mu(x)]\psi_1(x) \\ D_\mu\psi_2(x) &\equiv [\partial_\mu - ig'y_2B_\mu(x)]\psi_2(x) \\ D_\mu\psi_3(x) &\equiv [\partial_\mu - ig'y_3B_\mu(x)]\psi_3(x) \end{aligned} \quad (2.6)$$

where,  $\sigma^i$  are the Pauli spin matrices and  $B_\mu$  represents a field imposed by an external source. We find that,

$$\begin{aligned} \widetilde{W}_\mu(x) &\equiv \frac{\sigma_i}{2} \left\{ \partial_\mu W_\nu^i - \partial_\nu^i + g\epsilon^{ijk}W_\mu^jW_\nu^k \right\} \\ B_{\mu\nu} &\equiv \partial_\mu B_\nu - \partial_\nu B_\mu \end{aligned} \quad (2.7)$$

The Lagrangian now satisfies  $SU(2) \otimes U(1)$  symmetry between all gauge fields as shown in equation 2.8. It should be noted that the fermion fields and gauge bosons are required to be massless. This does not accurately describe the true interaction since 3 of the 4 gauge bosons are known to have mass, but the theory does allow an interface between neutrino interactions in the standard model.

$$\mathcal{L} = \sum_{j=0}^3 i\bar{\psi}_j(x)\gamma^\mu D_\mu\psi_j(x) \quad (2.8)$$

From equation 2.8, the terms that account for interaction of gauge bosons with the fermion fields are shown below in equation 2.9

$$\mathcal{L} \rightarrow g\bar{\psi}_1(x)\gamma^\mu\widetilde{W}_\mu\psi_1(x) + g'B_\mu\sum_{j=0}^3 y_j\bar{\psi}_j(x)\gamma^\mu\psi_j(x) \quad (2.9)$$

From this, we are then able to construct the Lagrangian for both the charged and neutral currents. The charged current Lagrangian is shown in equation 2.10.

$$\mathcal{L}_{CC} = \frac{g}{2\sqrt{2}} \left\{ W_\mu^\dagger [\bar{q}\gamma^\mu(1-\gamma_5)q' + \bar{\nu}\gamma^\mu(1-\gamma_5)\bar{l}] + \dots \right\} \quad (2.10)$$

The neutral current term in the Lagrangian contains gauge fields for both the Z boson and photon, which can be broken into two terms to account for a non-zero Z boson mass while leaving the photon massless through spontaneous symmetry breaking (SSB). This is done through an arbitrary rotation, as shown in equation 2.11, where  $\theta_w$  is known as the Weinberg or weak mixing angle. This angle is important because it is the angle used to rotate through SSB giving the Z boson its mass.

$$\begin{pmatrix} W_\mu^3 \\ B_\mu \end{pmatrix} = \begin{pmatrix} \cos \theta_w & \sin \theta_w \\ -\sin \theta_w & \cos \theta_w \end{pmatrix} \times \begin{pmatrix} Z_\mu \\ A_\mu \end{pmatrix} \quad (2.11)$$

It is then possible to write the neutral current Lagrangian that accounts for the interaction of the Z boson as shown in equation 2.13.

$$\mathcal{L}_{NC} = \frac{e}{2\sin(\theta_w)\cos(\theta_w)} Z_\mu \sum_f \bar{f}\gamma^\mu(v_f - \alpha_f\gamma_5)f \quad (2.12)$$

where,

$$g\sin(\theta_w) = g'\cos(\theta_w) = e \quad \text{and} \quad \cos(\theta_w) = \frac{M_w}{M_z} \quad (2.13)$$

The neutral current coupling constants,  $v_f$  &  $\alpha_f$ , differ with respect to the various quark, charged and neutral lepton fields. The neutrinos can be described as interacting via the charged and neutral currents. The Feynman diagrams, shown in figure 2.4, depict how the leptons couple to the quarks via the current mediator.

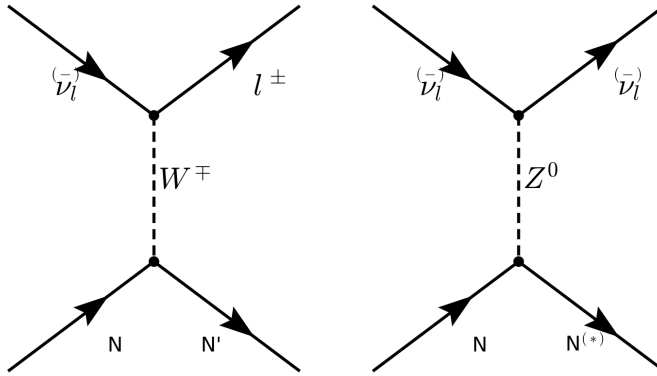


Figure 2.4: The Feynman diagram on the left describes a charged current (CC) neutrino interaction which transforms neutrinos into their corresponding charged leptons. In the CC interaction diagram the  $N \rightarrow N'$  represents a changed nucleon charge. The diagram on the right shows the neutral current(NC) neutrino interaction with preserves the neutrino while it interacts. In the NC interaction diagram the  $N \rightarrow N^*$  represents a same charge nucleon that could be at a higher resonance state.

## 2.5 Neutrino Mass and Flavor Oscillations

Neutrino oscillation is a quantum mechanical phenomenon in which the fraction of neutrino flavor changes while it propagates.[3] [4] This phenomena was first proposed in 1957 by Bruno Pontecorvo and relates the neutrino mass eigenstates with the flavor eigenstates through a rotation. This phenomena is best shown through a two neutrino flavor example, then extended into 3 flavors.

The mixing matrix for a two flavor neutrino case is:

$$\begin{pmatrix} \nu_e \\ \nu_\mu \end{pmatrix} = \begin{pmatrix} \cos \theta & \sin \theta \\ -\sin \theta & \cos \theta \end{pmatrix} \begin{pmatrix} \nu_1 \\ \nu_2 \end{pmatrix} \quad (2.14)$$

In this example, the flavor states are represented as  $\nu_e$  and  $\nu_\mu$  which are expressed as a mixture of mass states  $\nu_1$  and  $\nu_2$ . For aesthetic reasons, we chose  $\nu_\mu$  to be part of the example because most man made neutrino beams produce a relative pure sample of  $\nu_\mu$ . The framework for this example is commonly used as an oscillation approximation and can be generalized to satisfy any case of two distinctly different flavor neutrinos.

Using the two flavor formalism a pure  $\nu_\mu$  neutrino state can be expressed as equation 2.15

$$|\nu_\mu(0)\rangle = -\sin \theta |\nu_1(0)\rangle + \cos \theta |\nu_2(0)\rangle \quad (2.15)$$

The evolution of the state is governed by solving the time dependent Schrödinger equation for the initial muon state:

$$|\nu_\mu(t)\rangle = e^{-i\frac{Et}{\hbar}} |\psi(0)\rangle = -e^{-i\frac{E_1 t}{\hbar}} \sin \theta |\nu_1\rangle + e^{-i\frac{E_2 t}{\hbar}} \cos \theta |\nu_2\rangle \quad (2.16)$$

Assuming neutrinos travel near the speed of light, we rewrite equation 2.16 using the relativistic approximation, along with setting  $c = \hbar = 1$  and  $p_1 = p_2 = p$ :

$$|\nu_\mu(t)\rangle \simeq -e^{-i(p_1 + \frac{m_1^2}{2p_1})t} \sin \theta |\nu_1\rangle + e^{-i(p_2 + \frac{m_2^2}{2p_2})t} \cos \theta |\nu_2\rangle \quad (2.17)$$

with,

$$E = \sqrt{p^2 + m^2} = p \sqrt{1 + \frac{m^2}{p^2}} \approx p + \frac{m^2}{2p} \quad (2.18)$$

Next, the mass terms are grouped together and defined as the absolute square difference,  $\Delta m^2 \equiv |m_2^2 - m_1^2|$ . We find that if the mass are different then the mass eigenstates propagate at different frequencies and give rise the oscillatory behavior. The time dependent state can now be wrote as:

$$|\nu_\mu(t)\rangle = e^{-i\phi} (-\sin \theta |\nu_1\rangle + e^{+i\frac{\Delta m^2}{2p}t} \cos \theta |\nu_2\rangle) \quad (2.19)$$

with,  $e^{-i\phi} \equiv e^{-i\left(p + \frac{m_1^2}{2p}\right)t}$

To calculate the probability of the initial  $\nu_\mu$  state being measured as a  $\nu_e$  state at some later time  $t$ , we need to calculate the absolute value squared of the overlap between the states. Utilizing the relationship  $\langle \psi_i | \psi_j \rangle = \delta_{i,j}$ , the overlap between the states is:

$$\langle \nu_e | \nu_\mu(t) \rangle = e^{-i\phi} (-\sin \theta \cos \theta + \sin \theta \cos \theta e^{i\frac{\Delta m^2}{2p}t}) \quad (2.20)$$

The probability reduces to:

$$\begin{aligned}
 P(\nu_\mu \rightarrow \nu_e) &= |\langle \nu_e | \nu_\mu(t) \rangle|^2 \\
 &= e^{i\phi} e^{-i\phi} \sin^2 \theta \cos^2 \theta (-1 + e^{-i\frac{\Delta m^2}{p}t})(-1 + e^{+i\frac{\Delta m^2}{p}t}) \\
 &= \frac{1}{2} \sin^2 2\theta \left( 1 - \cos \left( \frac{\Delta m^2}{2p} t \right) \right)
 \end{aligned} \tag{2.21}$$

Finally, from relativistic assumptions, we set  $p = E_\nu$  as the outgoing neutrino energy and  $t = L$  corresponds to the distance traveled.

$$P(\nu_\mu \rightarrow \nu_e) = \sin^2 2\theta \sin^2 \left( \frac{\Delta m^2 L}{4E_\nu} \right) \tag{2.22}$$

From a proper accounting of numerical values of  $c$  and  $\hbar$ , equation 2.22 is more commonly written as:

$$P(\nu_\mu \rightarrow \nu_e) = \sin^2 2\theta \sin^2 \left( 1.27 \frac{\Delta m^2 L}{E_\nu} \right) \tag{2.23}$$

This oscillation behavior is best visualized as a plot of the probability of appearance and disappearance as shown Figure 2.5.

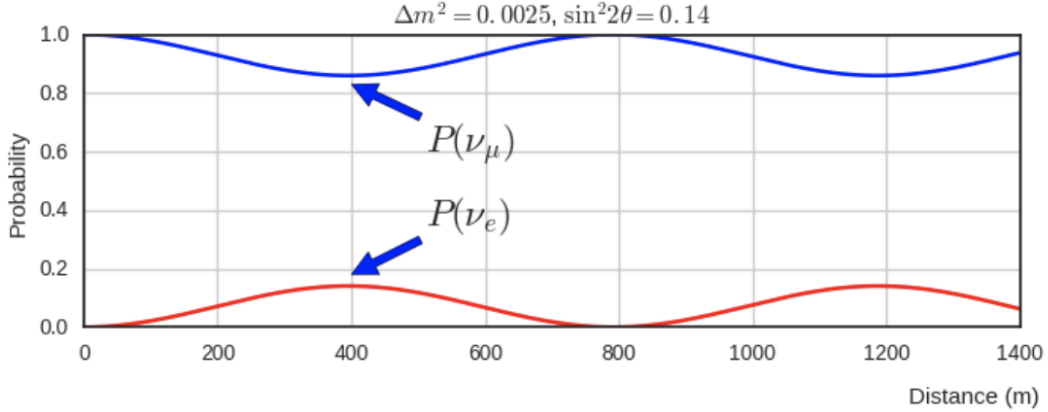


Figure 2.5: This plot shows the appearance and disappearance curves for a 2-flavor approximation as a function of baseline. The values of  $\Delta m^2 = 0.0025 \text{ eV}^2$  and  $\sin^2 \theta = 0.14$  are used.

As shown prior from figure 2.2, there are very good constraints on the number of active neutrinos[5]. Extending this formalism to a 3 flavor case was done by Pontecorvo-Maki-Nakagawa-Sakata (PMNS). The PMNS matrix is a 3 dimensional unitary matrix which is parameterized by three mixing angles  $\theta_{12}, \theta_{23}, \theta_{13}$  a complex phase  $\delta$ . The three angle correspond to the mixing effect, while  $\delta$  is known as the charge parity (CP) phase. If the CP-phase is non-zero, then neutrinos violate charge parity conservation which leads to the conclusion that neutrinos and anti-neutrinos interact differently with matter. The value for  $\delta$  has yet to be observed.

$$U_{PMNS} = \begin{pmatrix} 1 & 0 & 0 \\ 0 & c(\theta_{23}) & s(\theta_{23}) \\ 0 & -s(\theta_{23}) & c(\theta_{23}) \end{pmatrix} \begin{pmatrix} c(\theta_{13}) & 0 & s(\theta_{13})e^{-i\delta} \\ 0 & 1 & 0 \\ -s(\theta_{13})e^{i\delta} & 0 & c(\theta_{13}) \end{pmatrix} \begin{pmatrix} c(\theta_{12}) & s(\theta_{12}) & 0 \\ -s(\theta_{12}) & c(\theta_{12}) & 0 \\ 0 & 0 & 1 \end{pmatrix} \quad (2.24)$$

where  $c(\theta_{ij}) \equiv \cos \theta_{ij}$  and  $s(\theta_{ij}) \equiv \sin \theta_{ij}$ . The matrix equation is now put into a more compact manor that relates the mixing of the 3 neutrino generations.

$$\begin{pmatrix} \nu_e \\ \nu_\mu \\ \nu_\tau \end{pmatrix} = \begin{pmatrix} U_{e,1} & U_{e,2} & U_{e,3} \\ U_{\mu,1} & U_{\mu,2} & U_{\mu,3} \\ U_{\tau,1} & U_{\tau,2} & U_{\tau,3} \end{pmatrix} \begin{pmatrix} \nu_1 \\ \nu_2 \\ \nu_3 \end{pmatrix} \quad (2.25)$$

In its most general form, the oscillation probability is:

$$P(\nu_\alpha \rightarrow \nu_\beta) = \delta_{\alpha,\beta} - 4 \sum_{j>i} U_{\alpha,i} U_{\beta,i} U_{\alpha,j}^* U_{\beta,j}^* \sin^2 \left( 1.27 \frac{\Delta m_{ij}^2 L}{E_\nu} \right) \quad (2.26)$$

From equation 2.26, we see that the oscillation probability is depended on the mass difference between states. Currently, there are no successful direct measurements of any given neutrino mass state. Therefore, there is an allowed ambiguity in the mass ordering of all three neutrino states. This is called the neutrino hierarchy problem. However, we do know that the difference between  $m_1$  and  $m_2$  is small relative to  $m_3$ . Using this, we can build a picture of the fraction of different flavor eigenstates corresponding to their various mass states for both types of hierarchy.

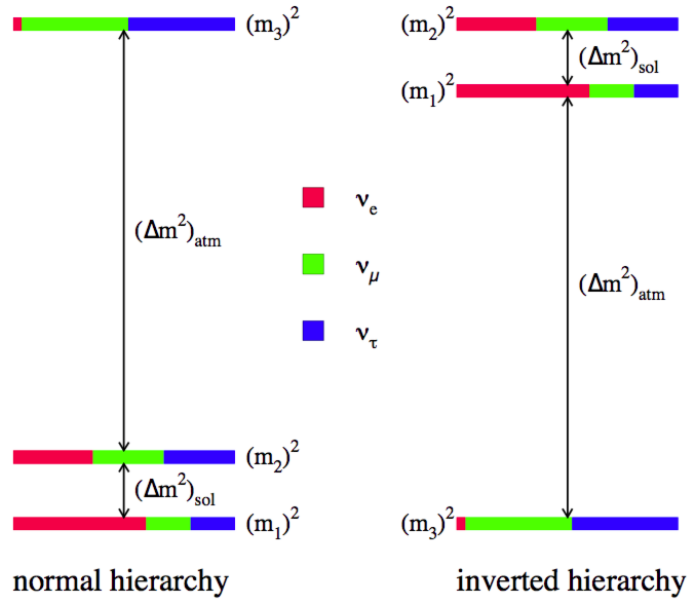


Figure 2.6: The two possible ordering for the 3 active neutrino mass eigenstates.

Many experiments have measured various elements of the PMNS matrix with neutrinos coming from accelerators, reactors, and solar sources. Currently, normal hierarchy ( $m_1 < m_2 < m_3$ ) is favored. Therefore, we will show (table 2.27) the current Particle Data Group (PDG)[6] best fit values for oscillation parameters with respect to normal hierarchy.

$$\begin{aligned}
\Delta m_{21}^2 &= 7.37 \times 10^{-5} eV^2 \\
\Delta m_{32}^2 &= 2.50 \times 10^{-3} eV^2 \\
\sin(\theta_{12}) &= 0.297 \\
\sin(\theta_{23}) &= 0.437 \\
\sin(\theta_{13}) &= 0.0214 \\
\delta/4 &= 1.35
\end{aligned} \tag{2.27}$$

## 2.6 Sterile Neutrinos

It is well accepted, from measurements at LEP[7], that there are only 3 neutrinos that couple through the weak interaction. Mathematically, nothing prohibits a theory that allows for neutrino mixing with other neutrino states beyond the 3 active states. These states, since they do not interact weakly, are called 'sterile neutrinos'. Extending the 3 flavor oscillation model to include any number of sterile neutrinos may be a possibility to address some the currently unexplained results in the neutrino physics fields. Each additional state requires an extra dimension to be added to the PMNS matrix. The sterile eigenstates are then defined as

$$|\nu_{s_i}\rangle = \sum_j^{3+N} U_{s_i,j} |\nu_j\rangle \quad (2.28)$$

where N is the number of sterile neutrinos.

The necessity for additional sterile neutrinos was prompted by the LSND experiment and later supported by the MiniBooNE. experiment. Both experiments are explained in depth in chapter 5. Each experiment found an excess of electron-like events at low energy. This suggested a  $\Delta m^2$  parameter space observed to be  $1\text{eV}^2$  larger than expected and strongly contradicted the results of many other results which had  $\Delta m^2$  around  $\mathcal{O}(10^{-3}\text{eV}^2)$  and  $\mathcal{O}(10^{-5}\text{eV}^2)$ . Proposing one or more sterile neutrinos could help explain the new different value of  $\Delta m^2$ . Adding more eigenstates in superposition during propagation allows for changes in the neutrino oscillation probabilities. The addition of extra sterile neutrinos and their effects are shown in the hierarchy plot in figure 2.7

The large  $\Delta m^2$  fit precipitated the need for further exploration of the LSND and MiniBooNE claims with more sophisticated detector technologies. The MicroBooNE experiment was proposed in 2001 and will be the focal point for this thesis.

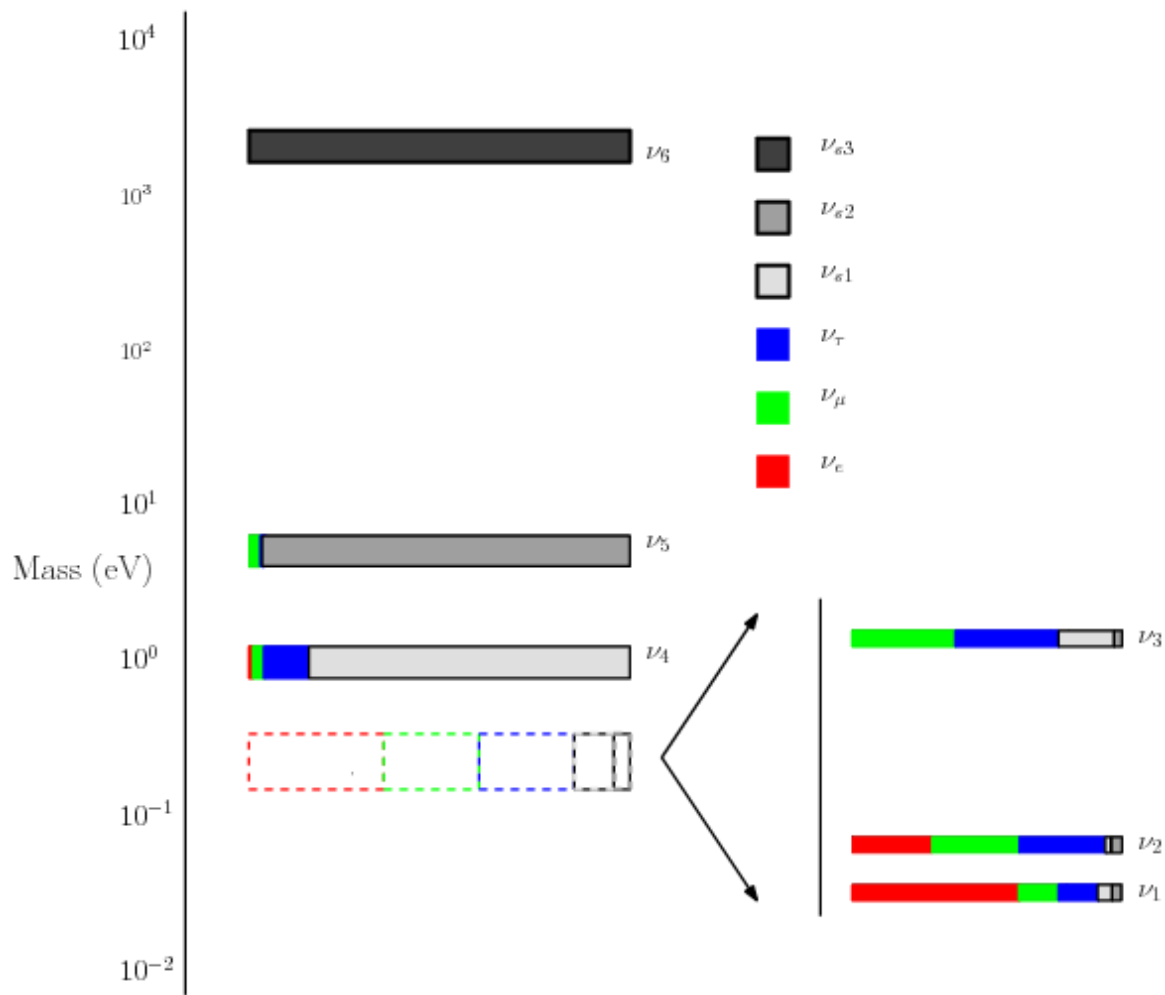


Figure 2.7: Mass hierarchy with potentially heavier sterile neutrinos.  $\nu_1, \nu_2, \nu_3$  represent the three current active neutrinos.  $\nu_4$  represents where the mass would be if fitting to LSND.  $\nu_5$  and  $\nu_6$  represent hypothetical heavier existing sterile neutrino mass states.

## Chapter 3

# The MicroBooNE Detector

### 3.1 Brief History of LAr-TPCs

The surprising nature of neutrinos quickly prompted the need for precision measurements of their interactions. Unfortunately, the low neutrino cross section posed a hurdle to build a high statistics detector. In 1977, C.Rubbia propose a Liquid Argon Time Projection Chamber (LArTPC) as large, high precision neutrino detector.[8] In 2001, The ICARUS collaboration commissioned the T600 detector which was one of the first large scale LArTPC's to be used as a neutrino detector. [9] The T600, which is comprised of 760 tons of liquid argon was commissioned in Pavia, Italy using cosmic rays as a proof of principle. Later the T600 was place underground in Hall B of Laboratori Nazionali del Gran Sasso (LNGS) which is located 730 km from the source of the CERN neutrino beam.

In 2009, the ArgoNeut collaboration, commissioned a small LArTPC in a 175 liter vacuum jacketed cryostat. The ArgoNeut TPC was comprised of 3 wire planes and operated at a drift field of 500 V/cm. The detector was placed just in front of the MINOS near detector in the NuMI beam at Fermi National Accelerator Laboratory (FNAL)[10]. ArgoNeut collected thousands of neutrino and anti-neutrino events providing valuable physics data and detector R&D for future experiments with LArTPC's.

The MicroBooNE (the Micro Booster Neutrino Experiment) detector, which will be discussed in depth throughout this chapter, is the first multi-ton LArTPC to be fully operational in the U.S.[11] The MircoBooNE detector design pioneered many new detector

R&D concepts such as: the ability to maintain high LAr purity in an unevaluated vessel, implementation of low noise electronic readouts at liquid cryogenic temperatures and advances in reconstruction techniques. MicroBooNE also supports a robust, high statistics physics program to address the MiniBooNE Low Energy Excess [12] and various cross section measurements. MicroBooNE was commissioned and began taking cosmic ray data in the summer of 2015. In October 2015 it began taking neutrino data. Shortly there after, the first neutrino event candidates were identified. [13]

## 3.2 Introduction

The MicroBooNE detector utilizes 170 tons of liquid argon to sustain 87 tons of active detector mass.[14] It is located at the Liquid Argon Test Facility (LArTF) which is 470 m downstream of the Booster Neutrino Beamline (BNB) source at the Fermilab National Accelerator Lab (FNAL) in Batavia, Illinois. The detector is the first large scale LArTPC to be deployed, commissioned and fully operated in the U.S.

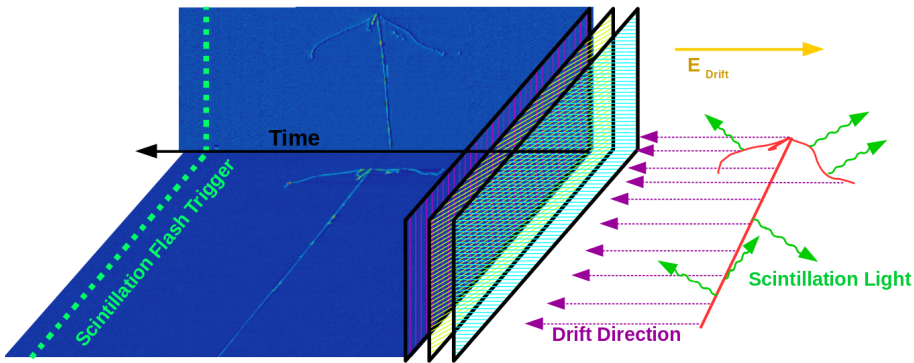


Figure 3.1: This diagram illustrates how a TPC works. First, charged tracks ionize the argon. The ions produce prompt scintillation light and the corresponding electrons begin to drift towards the wires due to the presence of the electric field. When the drift electrons reach the wire planes a 2D image is produced for each plane. When combining the 2D images from multiple planes along with the scintillation light information a 3D reconstruction is possible.

The general principle of a LArTPC involves utilizing two properties of LAr, scintillation

light and ionization. Charged particles travel through the argon and produce scintillation light which is collected by photomultiplier tubes (PMT's). A uniform electric field is applied over the active volume which transports the ionization electrons to a series of wire planes. Assuming the argon is pure and has minimal electro-negative contaminants, the wire planes then measure the induced or collected charge signal from the drifting electrons. The planes are each oriented at a different pitch angles. Each plane can then produce a two-dimensional image of the event as a function of wire and time. Combining multiple planes along with the PMT information allows for the object to be fully reconstructed in three dimensions. A diagram of the TPC concept is show in Figure 3.1. In the following sections the TPC, light collection system, and electronics are described in detail.

### 3.3 Time Projection Chamber

The TPC is the core of the MicroBooNE detector and forms a rectangular prism with dimensions  $2.3\text{ m} \times 2.6\text{ m} \times 10.4\text{ m}$  which contains 87t of LAr. The longest dimension, which in MicroBooNE's coordinate system is referred to as the z-direction, is oriented along the axis of the BNB. The majority of the TPC materials are composed of 304V stainless steel and G10. Stainless steel was chosen due to its low magnetic susceptibility, resistance to corrosion/oxidation, and ability to maintain its strength in cryogenic temperatures. G10 was chosen due to it's ability to perform well as an insulator in cryogenic environments.



Figure 3.2: The MicroBooNE TPC is shown here. On the far right is the flat cathode plane. The far left shows the 8,456 anode wires installed. The field cage tubes, which provide the uniform electric field, span the length between the anode and cathode.

The TPC field cage, which provides the uniform electric field through the detector volume, and was designed to produce field strengths up to 500 V/cm in liquid argon. The field cage consists of a total of 64 stainless steel rectangular loops that are supported and evenly spaced by a G10 holder. The cathode plane is a series of flat stainless steel sheets that is opposite the anode sense wires. Figure 3.2 shows the MicroBooNE TPC.

Every piece that was used in the MicroBooNE detector was thoroughly cleaned. Many pieces were cleaned in an ultrasonic cleansing bath while others were cleaned by hand. The detector was constructed in a clean environment that maintained positive pressure to mitigate the accumulation of dust. A complete description of the process is summarized in a separate technical note. [15]

MicroBooNE has a total of 8,465 sense wires that form 3 unique wire planes, one vertical collection plane (Y) and two induction planes (U,V) oriented at  $\pm 60^\circ$  relative to the Y plane. The wire planes are separated by 3 mm. The wires in each plane are evenly spaced by 3 mm pitch on carrier boards. The Y plane consists of 3,456 wires with a total of 108 carrier boards that accommodate 32 wires each. Each of the U and V planes consist of 2,400 wires with a total of 150 carrier boards that accommodate 16 wires each. The wires themselves are made of 304V stainless steel and are  $150 \pm 5 \mu\text{m}$  in diameter. A  $2\mu\text{m}$  layer of copper is plated over the wires to decrease the resistivity from  $40 \Omega/\text{m}$  to  $3 \Omega/\text{m}$ . The reduced

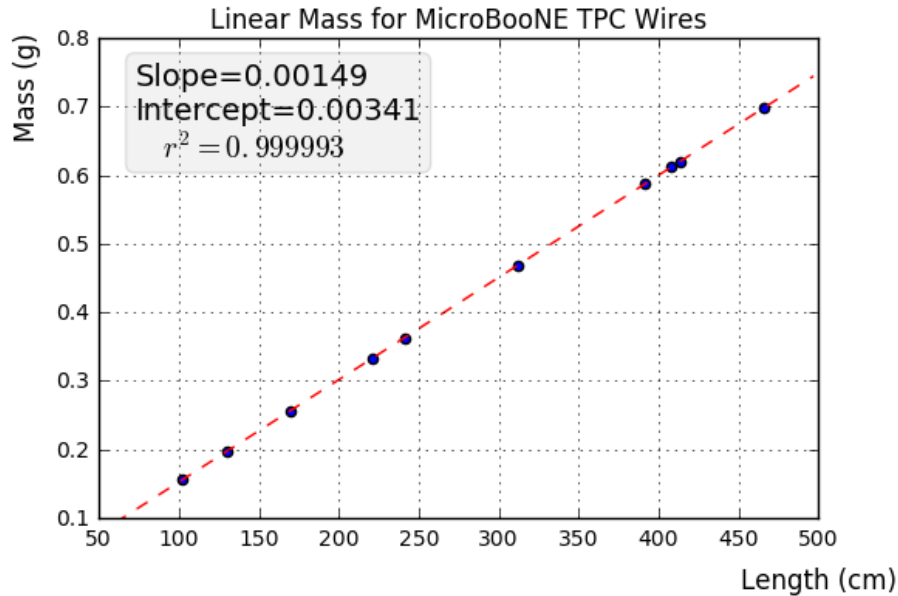


Figure 3.3: This plot is for a small sample used to cross check the linear mass density measured from the wire dealer. The slope from this plot represents the linear mass density and was found to be consistent with the value  $0.149\text{g/m}$ . The linear mass density is important to properly account for the wire tension of each wire.

resistivity aids in noise reduction at cryogen temperatures. Finally the wire is covered in and outer layer  $0.1\mu\text{m}$  of gold to prevent the copper from oxidizing over time. The linear mass density of a small sample of wires was measured and is shown in figure 3.3.

The wires were designed to installed at a nominal tension of  $6.97\text{ N}$ . To account for this, the carrier boards were installed onto a series of tensioning bars on the anode frame. These tensioning system, as shown in figure 3.4, allowed for fine tune adjustments to be made to separate sections of wires.

There are a total of 12 tensioning bars, 2 sets of 5 that traverse the entire top and bottom length of the anode frame, and 2 spanning the entire height of the upstream and downstream sections of the anode frame. Bronze jacking screws were used for final adjustments once all the wires were installed. Bronze was chosen since it has a similar thermal expansion coefficient to stainless steel and it is a softer metal which helps mitigate the risk of cold welding with stainless steel during the tensioning process.

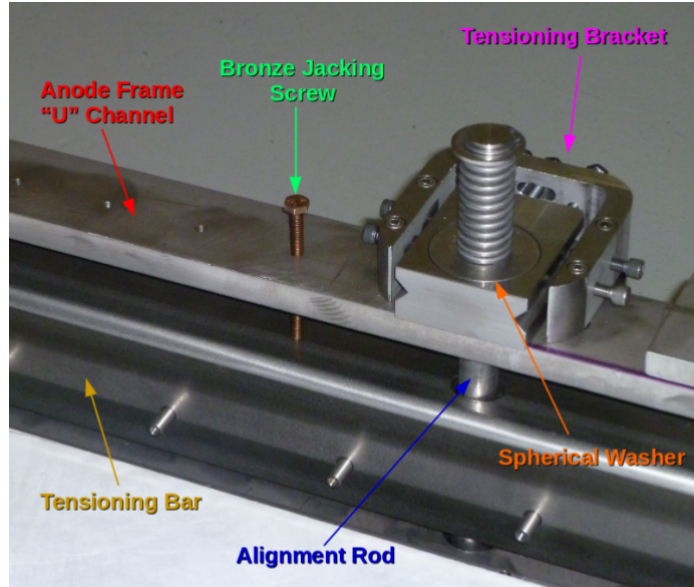


Figure 3.4: The MicroBooNE tension system. Wire carrier boards (not shown here) are mounted on the tensioning bar. The tensioning bar is able to move the wires during the tensioning process. Bronze jacking screws were used for final alignment during the tensioning process

In preparation for installing the actual detector wires, an installation team was trained on how to properly handle and install them. A 'mock-wire' installation was done to practice and identify the risks. After this, the actual wires were installed. The installation took approximately one week. The wires were installed serially, first the Y-plane, then the U-plane, and then the V-plane. After all the wires were installed, a G10 cover board was placed over carrier boards to secure and protect the electronics on the board, as shown in figure 3.5.

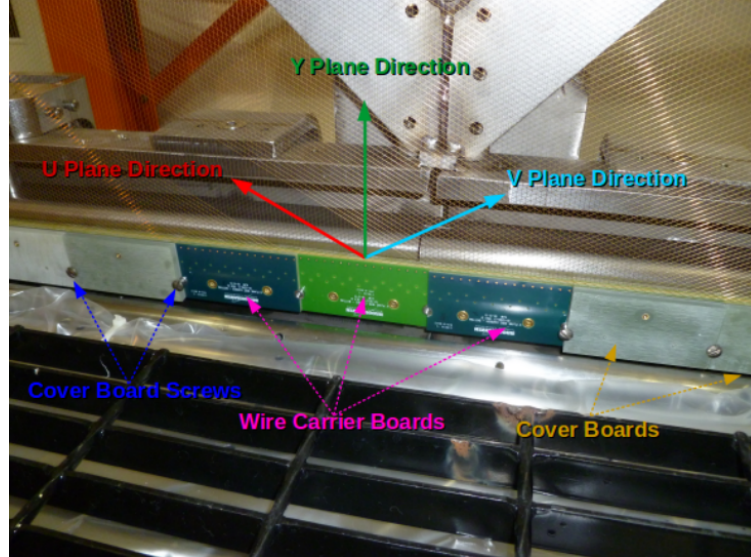


Figure 3.5: The MicroBooNE wires for 3 planes are shown here. The wire carrier boards are serially installed on the tensioning bar. The boards are held in place with a G10 cover plate that is secured with a smooth stainless steel screw.

Next, the wires were brought as close to nominal tension as possible. It was decided to favor under tensioning wires to minimize the risk of a broken wire during the tensioning process. The wire tensioning was done in a systematic way using the bronze jacking screws.

$$f = \frac{1}{2L} \sqrt{\frac{T}{\rho}} \quad (3.1)$$

Each wire has a characteristic resonance frequency that is related to its length, tension, and linear mass density through equation 3.1. A custom device was made to measure the resonant frequency of individual MicroBooNE wires. A laser light was focused on a particular wire and the wire gently plucked. A photo-diode mounted in an optical lens then measured the intensity of reflected light as the wire vibrated. The signals were then read into SpectrumAnalyzer, which is a software package that records frequency. SpectrumAnalyzer also allowed the high order frequency harmonics to be seen. The higher frequencies allowed for more precise tension measurement as seen in Figure 3.6

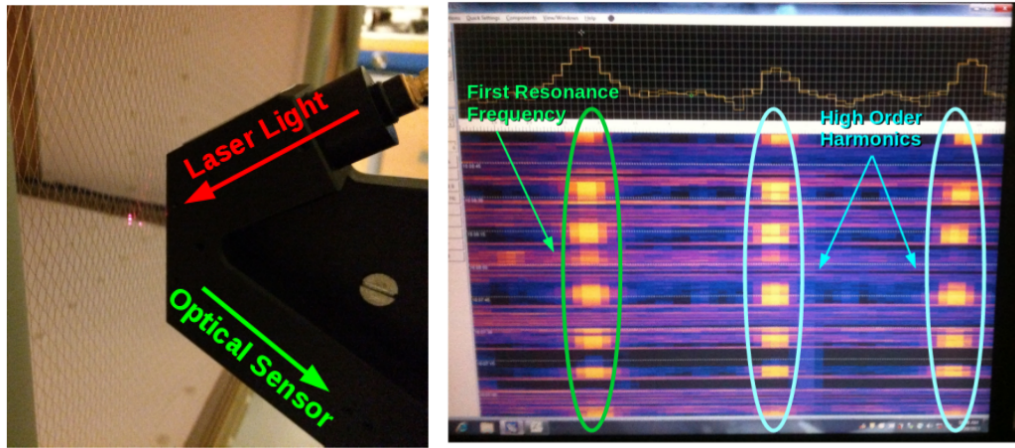


Figure 3.6: Left: Picture of the tension measuring apparatus including a laser and a optical sensor made of a photo-diode and a lens. Right: Example output of the SpectrumAnalyzer showing the first resonance frequency (bright line on the left) and the higher order harmonics (lines in the middle and right).

Note that the tension of 2328 out of 2400 U wires, 2308 out of 2400 V wires, and 3410 out of 3456 Y wires was measured, corresponding to 97.5 % of all wires installed in the detector. Only the wires inaccessible to the tension measuring device were not measured. The average tension for U,V,Y planes respectively was  $0.589 \pm 0.012$  kg,  $0.664 \pm 0.014$  kg,  $0.525 \pm 0.009$  kg. The tension for each plane is shown in Figure 3.7 and Figure 3.8.

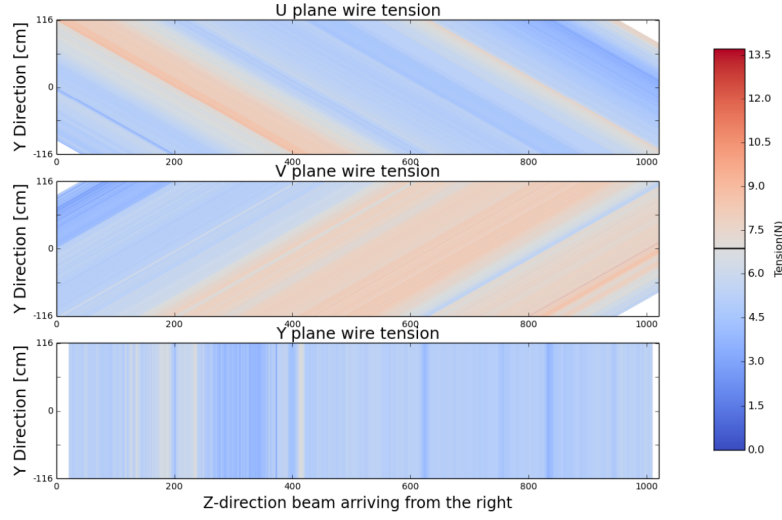


Figure 3.7: This a plane by plane map of the measured wire tensions for MicroBooNE. The tension was chosen such that each wire would not sag or come into contact with any adjacent wires.

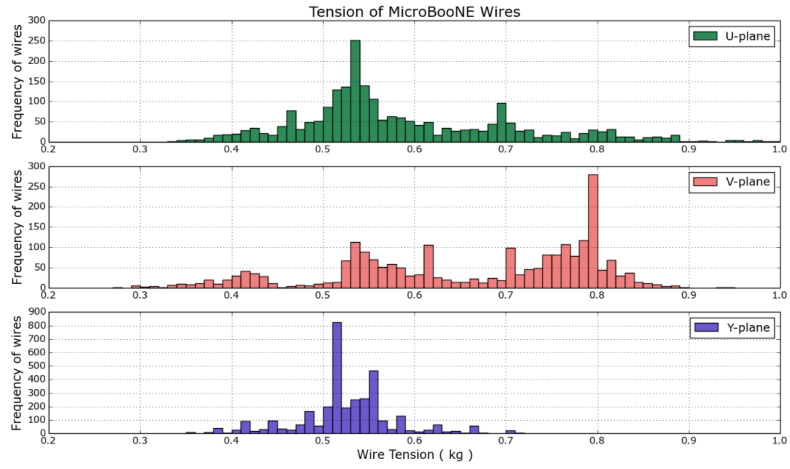


Figure 3.8: This a plane by plane histogram of the measured wire tensions for MicroBooNE.

### 3.4 Light Collection

The TPC can reconstruct 3D objects but there is still an ambiguity in the initial drift position. The light collection system in an LArTPC provides information to address this degeneracy. Scintillation light of liquid argon is 128nm wavelength and is produced through

two primary reactions. The first, which accounts for  $\approx 25\%$  of the light yield, is done through a  $\Sigma$  singlet excimer excitation and has a reaction time of  $6 \pm 2$  ns. This type of excimer is formed from an ionized argon atom that combines with another stable argon atom. The second, which accounts for the other  $75\%$  of light yield, is done through a  $\Sigma$  triplet excimer excitation and has a reaction time of  $1590 \pm 100$   $\mu$ s. The triplet state excimer is formed from a stable argon atom, an ionized argon atom, and a free electron. Since the prompt scintillation light is orders of magnitude faster than drift time from the TPC signal this information can be used to address this ambiguity.

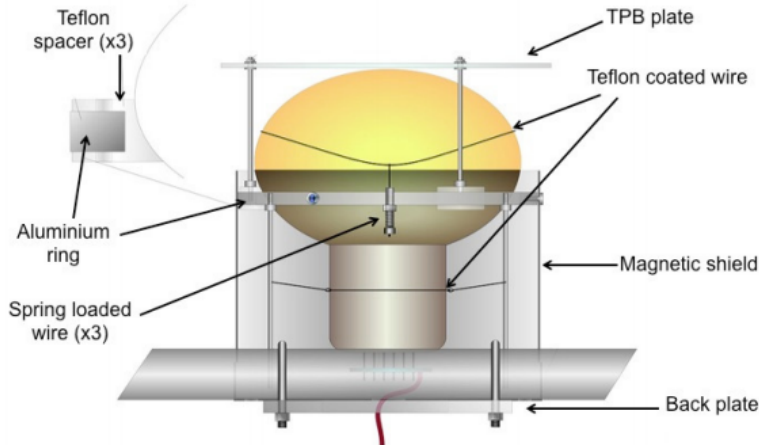


Figure 3.9: Schematic of a PMT optical unit for MicroBooNE.

The MicroBooNE light collection system consists of 32 8-inch diameter Hamamatsu R5912-02mod cryogenic PMTs. The PMT's are not optimized to detect 128nm light. Therefore, an acrylic plate coated with tetraphenyl butadiene (TPB)[16] was installed in front of the PMT's to act as a wavelength shifter. The TPB plate absorbs the 128nm light and re-emits at a peak wavelength of 425nm. Also, it is known that PMT response is reduced from certain orientations in the earth magnetic field. To address this a mu-metal shield was designed to extend just past the equator of the PMTs. A schematic of a PMT optical unit is shown in figure 3.9.

The PMT system is mounted on a railing behind the wire planes and spans the entire detector length as shown in figure 3.10. This also provides a weak handle on interaction

position since the scintillation light is fairly localized. Most importantly, since MicroBooNE is a surface detector and constantly being bombarded by cosmic rays, the scintillation flash is used as a method of identifying neutrino interactions coming in time with the beam.



Figure 3.10: PMT optical units installed on support racks inside the MicroBooNE cryostat

### 3.5 Electronics Readout

The TPC and PMT systems produce detector analog signals which need to be digitized, transferred out of the detector, and written to disk through data acquisition (DAQ) software. Both systems perform a first round of shaping and amplification in the cold LAr and then interface with warm electronics for further processing. The DAQ continuously writes to disk and creates a buffer which stores data for up to 24 hours. MicroBooNE employs various triggers to signify beam and non-beam data blocks and permanently store data from the buffer stream. A schematic overview of the TPC and PMT signal processing and readout stages is shown in Figure 3.11.

For the TPC, a large portion of the electronics processing for the 8,256 wire signals is performed directly in the LAr. To reduce electronics noise, the input distance from the wires to the preamplifier is minimized. The sense wires directly interface with CMOS analog front end ASICs which operate on cold motherboards. In total MicroBooNE has 516

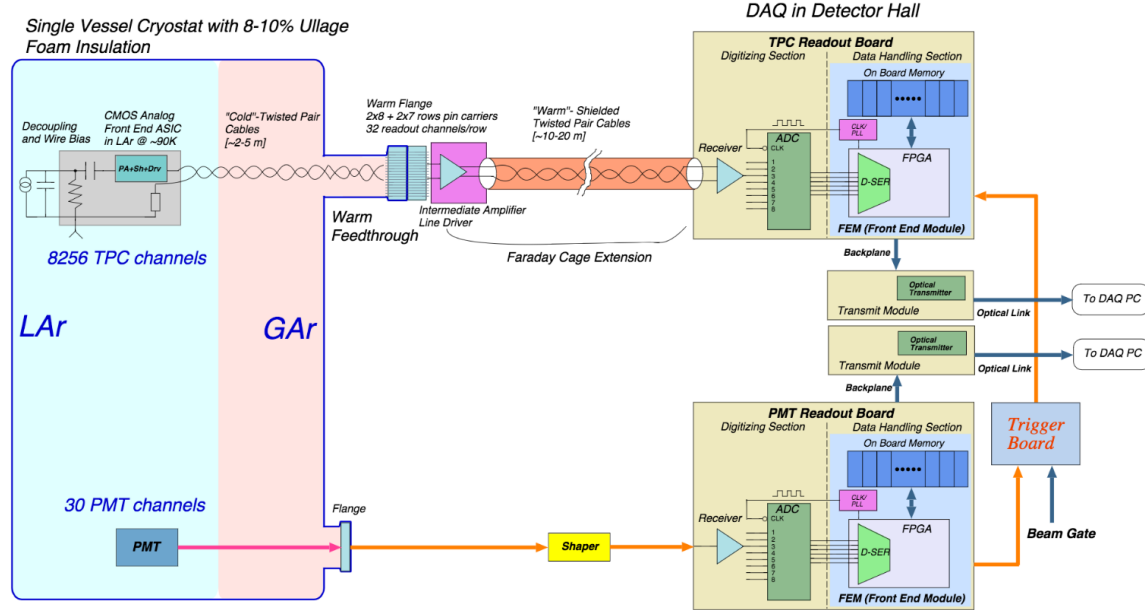


Figure 3.11: MicroBooNE LArTPC and PMT signal processing and readout schematic.

CMOS ASICs. The ASICs generate 50 W of heat load which is a negligible impact on the cryogenics system in order to prevent bubbles in the LAr. The motherboards shape and amplify the low noise signal. There are 36 top style motherboards that instrument Y, U and V plane wires and 14 side style motherboards that instrument U and V plane wires. The signals are then passed through a series of 12 feedthrough ports to warm electronics. The warm signals are then distributed over nine readout crates, which digitize the signals.

The TPC system read out frame is defined to be 1.6 ms. This number was chosen to account for ionization electrons that are generated at the cathode and drift the entire distance to the wires in the presence of a 500 V/cm E-Field. In MicroBooNE, an event is defined as four 1.6 ms readout frames. The additional frames allow for identification of cosmic particles that arrive before and after the neutrino interaction.

The PMT system is also processed in a similar fashion. The PMT's undergo 60 ns shaping to allow for precise measurements of the signal rising edge. The signals are sampled at 64MHz but only shaped signals above a threshold are read out and stored for data. The PMT signals are split into two different gains. A high gain signal that is 10 times the amplitude of the low gain. The signals are then brought to pre-amp/shaper boards and

digitized and sent to the DAQ.

## Chapter 4

# Booster Neutrino Beam

Fermilab is one of the world's leading neutrino facilities and currently produces two neutrino beams that span a wide range of neutrino energies. The Booster Neutrino Beam (BNB), which will be described in detail throughout this chapter, is a lower energy beam that delivers neutrinos to various short baseline experiments. Fermilab also hosts the NuMI (Neutrinos at the Main Injector) Beam which produces neutrinos over a large range between 1 GeV/c - 30 GeV/c and delivers neutrinos to various experiments both on-axis and off-axis. The NuMI beam will not be covered in this thesis.

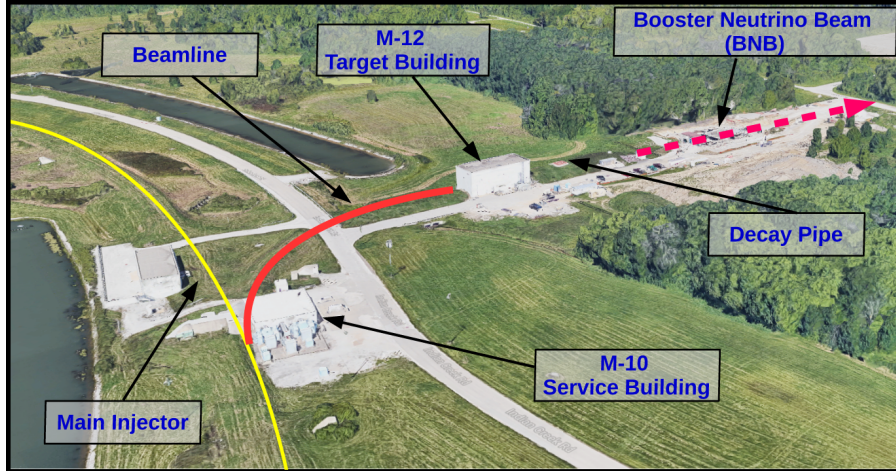


Figure 4.1: This image shows an aerial view of the Booster Neutrino Campus. Protons are extracted before the main injector near the M-10 service building and delivered to the M-12 target hall where the low energy neutrino beam is produced.

The Booster neutrino campus is illustrated in figure 4.1. To produce the BNB, protons are extracted from a transfer line just prior to the main injector and then interact with a beryllium target. The following sections will describe the beam system, neutrinos production process, and flux predictions for the BNB.

## 4.1 Primary Beam, Target and Horn

The BNB extracts 8.89 GeV/c momentum protons from the Fermilab Booster synchrotron and delivers them to a Beryllium target housed in the M-12 building. The protons from the booster are grouped in  $1.6 \mu\text{s}$  windows called 'beam spills'. One beam spill contains approximately  $5 \times 10^{12}$  protons. On average the Booster can run no more than 5 Hz with no more than 11 pulses in a row at 15 Hz. In optimal running conditions the Booster can deliver  $9 \times 10^{16}$  protons on target (P.O.T) per hour.

The beam pipe directly leading to the target is approximately 5 feet long and is held under vacuum to minimize proton interactions not originating from the target. The incoming proton flux is measured by a pair of toroids which are positioned upstream of the target and provide an error on P.O.T on the order of 2%.

The target consists of 7 cylindrical Beryllium slugs that together produce an effective cylinder of 71.1 cm in length and 0.51 cm in radius. The use of multiple slugs gave the Beryllium more surface area to allow efficient heat transfer from a simple air cooling system to be sufficient. An exploded view of the BNB target is shown in figure 4.2. As the protons collide with the beryllium, large amounts of secondary and tertiary mesons, such as  $\pi^\pm$  and  $K^\pm$ , are produced. These mesons will later decay into neutrinos and other decay particles.

The target is positioned inside of a large toroidal electromagnet called a horn. The horn is made of an aluminum alloy (6061 T6) and is pulsed with 174 kA of current to produces a  $1/R$  field where R is the distance from the axis of the horn. Since neutrinos are neutral particles they cannot be directly focused by an electric or magnetic force. Instead, the horn focuses the proper sign parent  $\pi^\pm, K^\pm$  in such a configuration that the neutrino angle from the parent decay particles are focused in a beam.

Directly downstream of the horn/target assembly is a collimator that is used to reduced

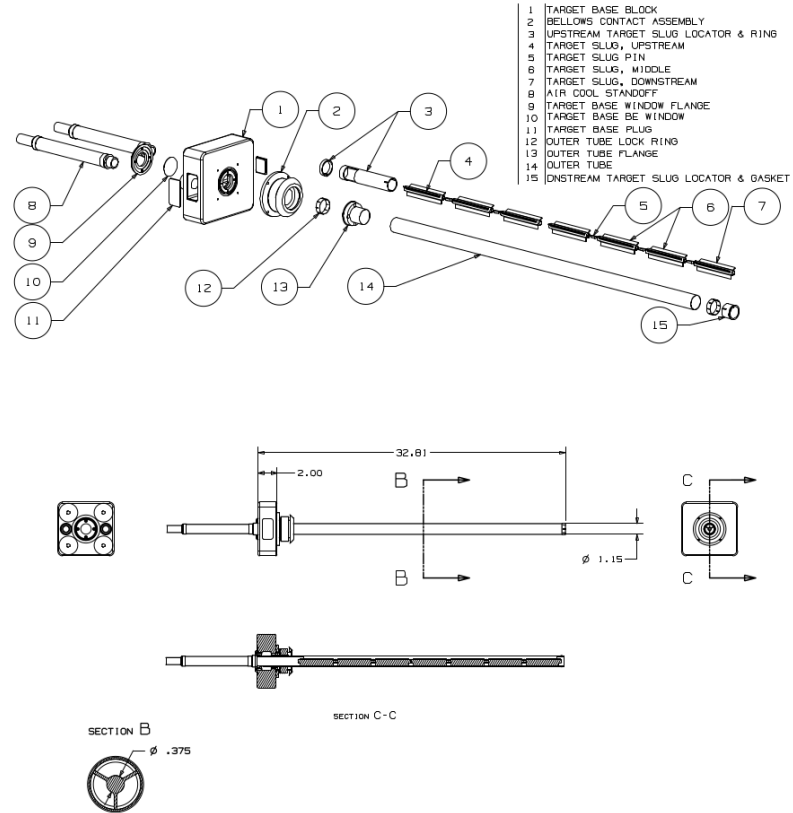


Figure 4.2: An exploded view of the BNB target which shows the 7 Beryllium slugs housed inside the support structure.

background coming from unwanted particles. Particles passing through the collimator enter a 45 m long decay region. In this region, most of the particles decay to produce the neutrino beam. At the end of the decay region there is a beam stop made of steel and concrete. There is also an array of gas proportional counters to detect high energy muons that punch through the beam stop. A diagram of the entire BNB system is shown in figure 4.3. When the horn polarity focuses (negative) positive charged mesons a (anti)neutrino beam is produced.

## 4.2 Neutrino Flux Prediction

The neutrino flux prediction for MicroBooNE uses the same GENIE simulation files used by MiniBooNE.[17] The files are feed into a Geant4 module that simulates the particles

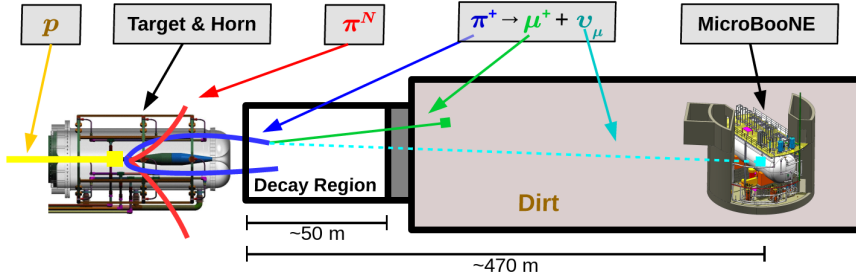


Figure 4.3: This figure shows the Booster Neutrino Beam line at FNAL. The neutrinos are produced in the decay region and then travel towards the MicroBooNE detector located 470 m down stream.

as they travel through the target, horn, and decay region. This produces a Monte Carlo (MC) flux estimate for each of the various neutrino types.[18] A systematics study was then performed to provide an error estimate for each of the  $\nu_e$ ,  $\bar{\nu}_e$ ,  $\nu_\mu$ , and  $\bar{\nu}_\mu$  flux predictions. To do this, 6 primary systematics were varied: the production rates of  $\pi^+$ ,  $\pi^-$ ,  $K^+$ ,  $K^-$ , and  $K_L^0$ , and a group systematic comprised of the horn current miscalibration, skin depth, nucleon inelastic, nucleon quasielastic(QE), nucleon total cross sections, pion inelastic, pion QE, and pion total cross sections. Beam errors for each of systematics are shown in Table 4.1 .The final flux estimate with the error uncertainty is shown in Figure 4.4.

	$\nu_\mu$	$\bar{\nu}_\mu$	$\nu_e$	$\bar{\nu}_e$
Delivered P.O.T.	2.00%	2.00%	2.00%	2.00%
$\pi^+$	5.8%	0.46%	4.62%	2.66%
$\pi^-$	0.01%	7.51%	0.28%	3.20%
$K^+$	0.38%	0.13%	5.19%	2.61%
$K^-$	0.01%	0.35%	0.28%	3.92%
$K_l^0$	0.03%	0.27%	2.36%	22.59%
Other	5.78%	6.09%	3.6%	7.61%

Table 4.1: Systematic errors for production of various neutrino types with respect to their, P.O.T. , parent particle, and other variables.

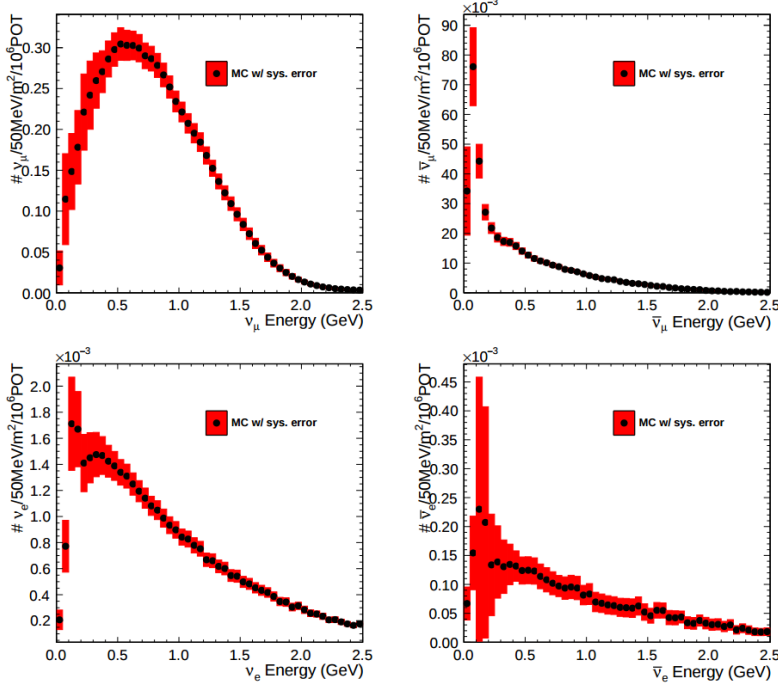


Figure 4.4: Monte Carlo flux predictions for the BNB neutrino spectrum. The red band represents the flux systematic errors. Note the orders of magnitude with the  $\nu_\mu$  spectrum rates.

## Chapter 5

# Low Energy Excess and Relevant Cross Sections

### 5.1 Overview

This chapter will discuss various facets of what is commonly called the “MiniBooNE Low Energy Excess.” First, we will present the anti-neutrino excess observed by LSND and how the oscillation results can be interpreted. Then, we will discuss the efforts of MiniBooNE to understand the LSND results along with their oscillation results that establish the “MiniBooNE Low Energy Excess.” We will also discuss the neutral current  $1\pi^0$  cross section which is the dominant background in the oscillation analysis claims for both MiniBooNE and LSND. Finally, we will discuss MicroBooNE’s role towards addressing understanding the low energy excess claims of MiniBooNE.

### 5.2 LSND Excess

The Liquid Scintillator Neutrino Detector (LSND) was a 167 ton neutrino detector stationed at Los Alamos National Lab (LANL) designed to study neutrino oscillations. The detector, which hosted 1220 PMT’s for event detection, was placed 30 m away from the source of a low energy ( 40 MeV)  $\bar{\nu}_\mu$  beam. Using the Los Alamos LAMPF beam, 800 MeV protons interacted with a water target to produce  $\pi^+$  mesons which decayed into  $\mu^+ + \nu_\mu$ . The  $\mu^+$

would then interact with a copper beam stop and decay at rest to produce the low energy  $\bar{\nu}_\mu$  beam.

The detector medium was primarily carbon (mineral oil  $CH_2$ ). LSND could easily distinguish between electromagnetic showers (electrons/positrons/photon) or tracks (pions/muons/protons) by differences in the Cherenkov cone that were produced. The oscillation signal interaction was  $p + \bar{\nu}_e \rightarrow n + e^+$ . The primary  $e^+$  is easily visible from the Cherenkov light it produced but a neutron would not have produced Cherenkov light and therefore be invisible to the detector. The organic scintillator b-PDB was dissolved in the mineral oil at a concentration of 31 mg/l. The scintillator allowed the 2.2 MeV photon from the capture of the neutron on hydrogen to be detected. This allowed LSND a unique signal to identify  $\bar{\nu}_e$  interactions. It should be noted that the detector technology could not easily discriminate between photons, electrons or positrons induced electromagnetic showers.

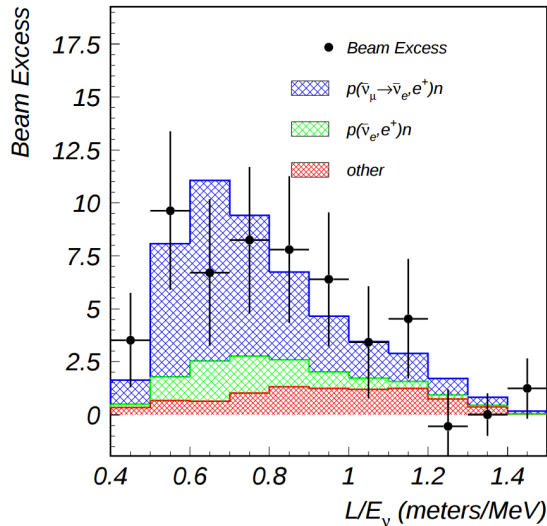


Figure 5.1: This is the LSND neutrino oscillation appearance plot as a function of  $L/E$  and represents the 87 event  $\bar{\nu}_e$  excess claimed by the experiment.

In 2001, the LSND collaboration published results for an observed excess of  $87 \pm 22.4$  statistical,  $\pm 6.0$  systematic events above the predicted background as shown in figure 5.1. If the excess is interpreted as neutrino oscillations from a two neutrino model, the best fit of the excess would suggest a  $\sin^2(2\theta) = 0.003$  and  $\Delta m^2 = 1.2\text{eV}^2$  which greatly contradicts many other measurements for  $\Delta m_{2,3}^2$  or  $\Delta m_{1,3}^2$  [19]. One explanation for the excess suggests the idea of mixing between other additional neutrino states. These neutrinos are called ‘sterile’ since they cannot directly couple via weak interaction as mentioned prior from the constraints from LEP.

### 5.3 MiniBooNE Excess

The Mini Booster Neutrino Experiment (MiniBooNE) was designed to address the claims of the LSND  $\bar{\nu}_e$  excess result. The MiniBooNE detector was a mineral oil Cherenkov detector designed to be a similar technology to LSND[20]. MiniBooNE, stationed at FNAL in the BNB, was positioned 541 m from the neutrino source and was able to receive both  $\nu_\mu$  and  $\bar{\nu}_\mu$  fluxes. The distance was chosen such that the  $L/E$  parameter were similar to that of the LSND experiment.

MiniBooNE, which contained 818 tons of mineral oil ( $CH_4$ ), was located underneath more than 3m of earth overburden to help reduce cosmic rays. The detector supported a 35 cm thick outer cosmic veto using 240 PMT’s. The veto efficiency was 99.99% for rejecting cosmic muons. The inside of the detector was instrumented with 1,280 8-inch PMT’s which were used to read out neutrino and comsic data. Cherenkov light from different particles produced distinct patterns on various PMT’s inside the spherical detector. A cartoon showing various type of signal topologies from the MiniBooNE detector is shown in figure 5.2. The detector energy scale was calibrated *in situ* by fitting various parameters from through going muons, decay Michel electrons, and  $\pi^0$  decays. A clear limitation of Cherenkov detectors is the inability to concretely distinguish between photon induced or electron induced showers.

The primary oscillation analysis for MiniBooNE was done ‘blind’ in an attempt to gain confidence from the physics community upon its findings[21]. The entire analysis was

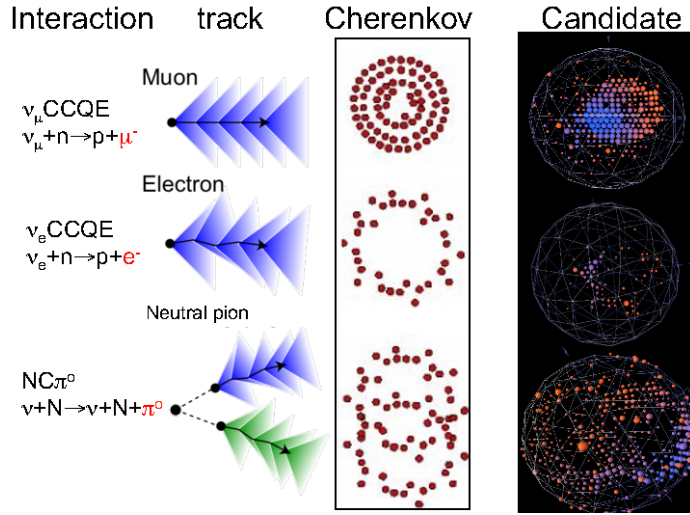


Figure 5.2: This cartoon depicts different particle interactions as observed in Cherenkov detector. The far right shows the interaction types as viewed in MiniBooNE

developed on large statistics Monte Carlo simulation and a small sample of test data. In total, MiniBooNE accumulated  $6.46 \times 10^{20}$  P.O.T. of  $\nu$ -data and  $11.27 \times 10^{20}$  P.O.T. of  $\bar{\nu}$ -data. Fermilab's ability to support both neutrino and anti-neutrino beams allow for MiniBooNE to confirm that an LSND-like excess was independent of neutrino type. The MiniBooNE data is in good agreement between signal and background predictions but contradicts the LSND claim up to 98% confidence in both modes above 500 MeV. The excess is most prominent in the region of events below 500 MeV, as seen in figure 5.3. In this region the largest background comes from  $\pi^0$ -misidentification followed by photons coming from radiative  $\Delta$  decays. MiniBooNE reports a total excess of  $240.0 \pm 62.9$  combined,  $(162.0 \pm 47.8\nu, 78.4 \pm 28.5\bar{\nu})$  events in the neutrino energy range  $200 < E_\nu^{QE} < 1250\text{MeV}$ . Also, if the excess is interpreted as a two flavor oscillation the inferred parameters are consistent with the LSND result.

## 5.4 Neutral Current $\pi^0$ Production

The leading background from the MiniBooNE oscillation result, as mentioned in chapter 5.3, is  $\pi^0$ -misidentification. Accurately measuring the neutrino induced neutral current single

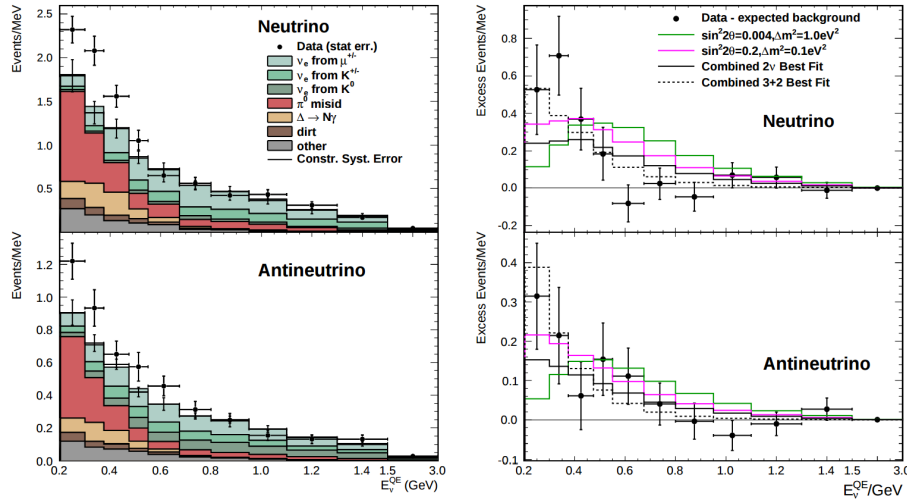


Figure 5.3: The left plots show the stacked histograms for signal and background overlaid with data for both neutrino and anti-neutrino modes. The right plots show the relative excess as a function of neutrino energy and make obvious the energy range that drives the excess.

$\pi^0$  production cross section is therefore crucial in understanding background contributions for an oscillation analysis. Charged current  $\pi^0$  production conveniently has an outgoing charged muon in the final state and is very easy to identify. On the other hand, neutral current  $\pi^0$  production does not guarantee any outgoing charged particles and therefore, makes identification much harder. For neutrinos in the BNB, the main production mode for neutrino induced neutral current  $\pi^0$  production is via the  $\Delta(1232)$  resonant production. Resonant production is when a baryon, such as a proton or neutron, is excited to a higher resonance state and then subsequently decays back to the initial state while liberating a  $\pi^0$ . There are other neutrino induced  $\pi^0$  production modes that MicroBooNE is sensitive to such as deep inelastic scattering and coherent production, but have a lower production cross section at the given BNB neutrino energy range. A general Feynman diagram can be used to describe the main components of neutrino induced neutral current single  $\pi^0$  production in argon as seen in Figure 5.4.

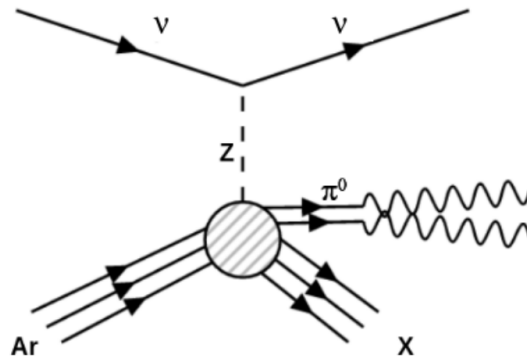


Figure 5.4: Neutrino induced single  $\pi^0$  production on argon. This topology is defined such that single  $\pi^0$  is produced and the other particles leaving the interaction ( $X$ ) must only consist of nucleons.

## 5.5 NC- $\pi^0$ in Carbon vs Argon

In 2010, MiniBooNE measured the total neutral current single  $\pi^0$  cross section on carbon with what is currently the world's largest statistics sample of  $\pi^0$ s. The MiniBooNE neutral current single  $\pi^0$  signal is defined as a topology that produces one and only 1  $\pi^0$  in the final state with no other other charged leptons or mesons originating from the vertex. In 2015, the first measurement of neutrino induced neutral current  $\pi^0$  production on argon was measured by ArgoNeut collaboration at Fermilab while running in the NuMI neutrino beam. AgroNeut, being a smaller detector, could not easily contain many of the electromagnetic showers from  $\pi^0$  decays. This forced the analysis choose a slightly different final state signal definition requiring there to be at least one  $\pi^0$ , no electron or muon, and allowing there to be any number of mesons in the final state. This modified signal definition makes any comparison to other historical data very complicated.

MicroBooNE, which resides in the same neutrino beam line as MiniBooNE, is a prime candidate for various studies of neutral current  $\pi^0$  production studies between different target materials (C/Ar). Being a larger LArTPC, more  $\pi^0$  decays will be contained allowing for high statistics measurements of the cross section along with the general need to measure the production rate as input to its own oscillation analysis.

## Chapter 6

# Cosmogenic $\pi^0$ s at MicroBooNE

In this chapter we will talk about some of the challenges and interesting physics cases regarding cosmogenics in a surface LArTPC. Many cosmic ray particles penetrate surface detectors and populate the detector region making it necessary to remove these particles from reconstruction and address charge contamination in neutrino events. The majority of this chapter will emphasize cosmogenic track removal, electromagnetic showers and subsequently  $\pi^0$  selection. We will first examine some historical cosmogenic studies from the Icarus experiment. Then, introduce what MicroBooNE can contribute in terms of understanding cosmics. We will address the cosmic simulation that is used, various steps in reconstruction and pattern recognition used to select  $\pi^0$ s in a LArTPC. Finally, we will conclude with how these studies impact future cross section analyses and backgrounds toward the low energy excess analysis.

### 6.1 Motivation

Cosmogenic particles allow for the separate test of reconstruction tools along with an independent way to address the detector energy scale. The high rate of surface cosmics cause some trouble with disentangling signal neutrino events from cosmic ray removal. Luckily, off beam surface cosmogenic samples allow for a large statistics dataset to develop and optimize reconstruction techniques. Cosmogenic muons that traverse the detector provide a handle to understand detector energy scale along with understanding track reconstruction

efficiency. Stopping muons that produce a Michel electron help provide a benchmark for low energy showers in the 10's of MeV range. The  $\pi^0$  resonance, with a mass of  $134.9 \text{ MeV}/c^2$ , can be used as a standard candle to benchmark overall detector energy scale. The calculated the  $\pi^0$  mass, as shown in equation 6.1, depends on a measurement of energy and photon opening angle.

$$\mathcal{M} = \sqrt{2E_1E_2(1 - \cos\theta_{12})} \quad (6.1)$$

Electromagnetic shower reconstruction for LArTPC's is well known to be a hard task. The high resolution of the 2-dimensional projections of EM-showers introduce many challenges to develop unbiased and fully automated reconstruction. In 2001, the T600 ICARUS detector [22] performed a surface test run in Pavia, Italy. During this 100 day test the detector collected over 30,000 cosmic ray events. In 2008, the ICARUS collaboration published a study of electromagnetic showers coming from  $\pi^0$  decays in the Pavia dataset. To select candidate  $\pi^0$  events, ICARUS hand scanned a total of 7,500 potential events from a PMT triggered sample. Their hand scanning requirements included, that at least two well separated electromagnetic showers were visible, a valid  $t_0$  time for the vertex, and that there was not much charge contamination coming from a nearby cosmic muon. After this, they were left with 212 hadronic interactions with at least one candidate neutral which they then proceeded to reconstruct. Their final reconstruction consisted of energy scaling to account for missing charge in the shower and a minimization against the true  $\pi^0$  mass. An example of one of their hand scanned clustering events is shown in Figure 6.1.

MicroBooNE, being a surface detector, is in a position to do a similar study with improved reconstruction techniques. Also, understanding the cosmic production rate for single  $\pi^0$ s is valuable to any MicroBooNE analysis that involves EM-showers. The following sections will present MicroBooNE's Monte Carlo simulation and state of the art reconstruction techniques.

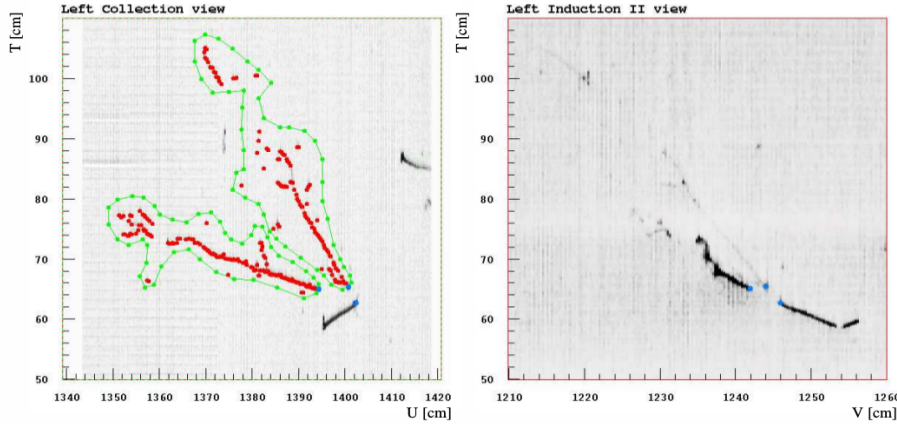


Figure 6.1: A cosmic  $\pi^0$  from the ICARUS Pavia run. The left image shows the hand drawn clustering and positions of the shower conversion point and vertex point. The right image shows the same event on a different wire plane view.

## 6.2 Traditional Reconstruction

The traditional approach for LArTPC reconstruction involves grouping drift charges that are deposited on the wires to form wire-hits. The light collection system also has light-hits which corresponded to collected light of an individual track or shower. A group of PMT's that have light-hits at the same time is called a flash. Hits from each of the wire planes are clustered together with various reconstruction algorithms to form reconstruction objects that relate to individual particles in the detector. There are two primary reconstruction objects: tracks, which are mostly linear and compact clusters that represent muons, protons, and charged pions, and showers which are more fuzzy shaped cluster objects that represent photons and electrons. Next, to reconstruct a 3D object, an algorithm must match the same 2D cluster objects in at least two of the three wire planes. For MicroBooNE, and the general LArTPC community, matching track reconstruction is well advance but shower reconstruction suffers many pitfalls. In recent years lots of progress has been made for LArTPC shower reconstruction. Various different techniques such as improved 2D clustering and matching techniques, sophisticated pattern recognition tools[23], and deep learning[24] approaches have been explored and each has its various strengths and weaknesses.

### 6.3 Wire Cell Imaging

The traditional approach is not the only way to reconstruct LArTPC data. Instead, wire data can be treated with a tomographic approach directly producing a set of 3D space points. Although computationally intensive, this approach allows for more information to be used in a 3D clustering framework which can directly impact shower reconstruction and mitigate degeneracies from the 2D matching method.

The Wire-Cell framework, spearheaded by Brookhaven National Labs (BNL), utilizes this approach to create 3D space points from MicroBooNE's TPC data. The approach relies on the assumption that the same amount of ionization charge is seen on each plane. In MicroBooNE this is done by reconstructing small time slices on each wire planes. Each time slice involves solving a charge equation for all possible hits with respect to the matrix of hits actually recorded in the time slice. The charge equation is shown in equation 6.2. The detector wire signals are represented in matrix  $W$  while all potential wire hits are contained in  $H$ . Nonzero values in the  $Q$  matrix will correspond to unique wire-plane intersections of charge, near zero values represent ghost hits due to degeneracies in the charge equation.

$$\begin{bmatrix} W_{u_1} \\ \vdots \\ W_{u_n} \\ W_{v_1} \\ \vdots \\ W_{v_n} \\ W_{y_1} \\ \vdots \\ W_{y_n} \end{bmatrix} = \begin{bmatrix} Q_{u_1}^{H_1} & Q_{u_1}^{H_2} & \dots & \dots & \dots & Q_{u_1}^{H_{m-1}} & Q_{u_1}^{H_m} \\ \vdots & \vdots & \ddots & \ddots & \ddots & \vdots & \vdots \\ Q_{u_n}^{H_1} & Q_{u_n}^{H_2} & \dots & \dots & \dots & Q_{u_n}^{H_{m-1}} & Q_{u_n}^{H_m} \\ Q_{v_1}^{H_1} & Q_{v_1}^{H_2} & \dots & \dots & \dots & Q_{v_1}^{H_{m-1}} & Q_{v_1}^{H_m} \\ \vdots & \vdots & \ddots & \ddots & \ddots & \vdots & \vdots \\ Q_{v_n}^{H_1} & Q_{v_n}^{H_2} & \dots & \dots & \dots & Q_{v_n}^{H_{m-1}} & Q_{v_n}^{H_m} \\ Q_{y_1}^{H_1} & Q_{y_1}^{H_2} & \dots & \dots & \dots & Q_{y_1}^{H_{m-1}} & Q_{y_1}^{H_m} \\ \vdots & \vdots & \ddots & \ddots & \ddots & \vdots & \vdots \\ Q_{y_n}^{H_1} & Q_{y_n}^{H_2} & \dots & \dots & \dots & Q_{y_n}^{H_{m-1}} & Q_{y_n}^{H_m} \end{bmatrix} \begin{bmatrix} H_1 \\ H_2 \\ \vdots \\ H_{m-1} \\ H_m \end{bmatrix} \quad (6.2)$$

Then, each ‘slice’ is stacked to its corresponding x position. This produces a set of 3D space points that can be used in pattern recognition algorithms to identify different particles in the data. All reconstruction is done with accounting for known detector dead regions. The current state of MicroBooNE’s signal and noise processing and imaging that requires a minimum of 2 wire planes to be matched from the charge equation.

## 6.4 Pattern Recognition

Various pattern recognition tools are needed to address MicroBooNE’s TPC data but for this analysis they can be generalized into two efforts, cosmic track removal and EM-shower clustering. Being that the Wire Cell imaging technique is a new approach, an independent analysis framework named Sp0ter was built. Sp0ter is written primarily in Python and leverages many common packages. The framework is able to ingest 3D space points from Wire Cell, clusters track and shower objects, and focuses on selecting and reconstruction single  $\pi^0$  events. First, we will focus on optimizing track removal. This involves identifying tracks that are through-going, and contained. Once all the charge associated with tracks are removed, the remaining charge is clustered into candidate EM-shower objects. Finally, correlated shower pairs are identified and selected as candidate  $\pi^0$  events.

A image of a typical MicroBooNE cosmic event reconstructed with 3D wire cell space points are shown in Figure 6.2 using the BEE viewer [25]. A detailed list of reconstruction and selection parameters are listed in the appendix.

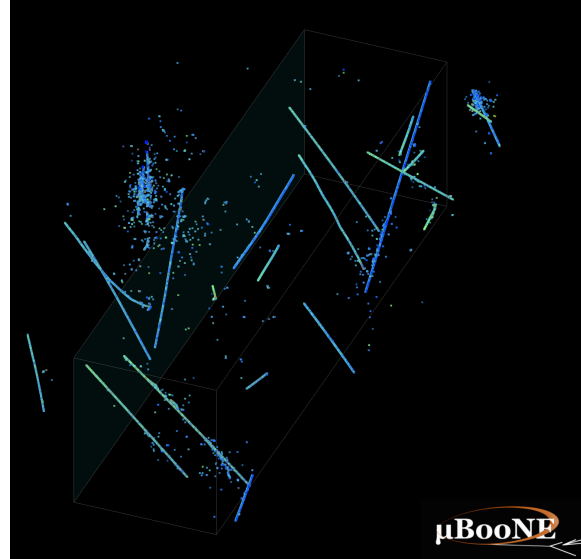


Figure 6.2: This is a typical cosmic event in the MicroBooNE detector. The data used to generate this event is CORSIKA Monte Carlo.

## 6.5 Clustering

The wire cell data produces a set of 3D space points as mentioned in section 6.3. Only space points that are in the fiducial volume are clustered and considered in the reconstruction process. First a charge threshold cut of 0.5 MeV is applied to all the remaining space points. This is to remove very low charge ghost points and reduce the overall number of points to cluster. The main goal of this step is to identify the large scale structure of the cosmic tracks in the data. Additionally, with a smaller number of space points the computational time for reconstruction is reduced.

The first stage of clustering uses BIRCH (balanced iterative reducing and clustering using hierarchies). The hyper parameters were tuned such that cosmic tracks are removed with minimal impact to showers involved from  $\pi^0$ . Birch clustering was chosen because it scales well with large number of points, efficiently maintains large number of clusters in datasets and also handles outliers removal well. This clustering technique leverages on the inherent structure of charged particle tracks having a well define 3-dimensional trajectory. Particles such as protons, muons, and charged pions are continuously ionizing meaning that there should be not be gaps in the detected charge. This feature is much different than

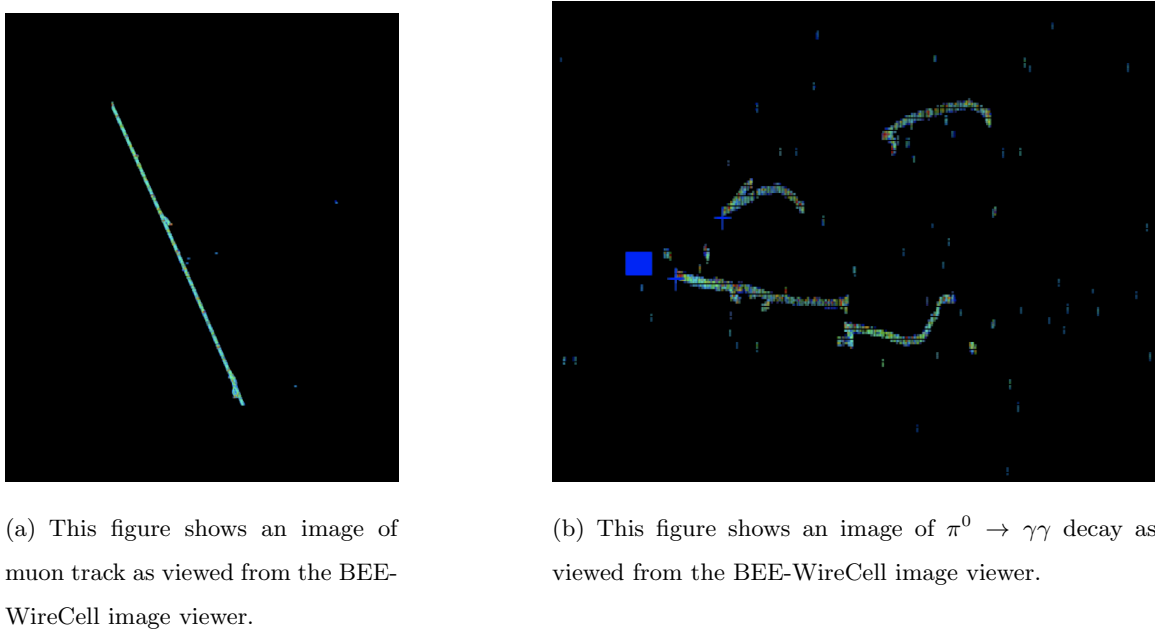


Figure 6.3: Images from the BEE-WireCell image viewer.

EM-showers which have lots of gaps between detected charge. An example of this is shown in section (b) of figure 6.5.

The next stage of the track and shower clustering process is to merge together proto-clusters that did not get fully grouped together in the BIRCH clustering step. The second pass clustering is geared toward larger object clustering. To address this, a 3D convex hull is constructed around every cluster. Next, the euclidean distance between all the vertex points are calculated. If the minimum merging distance is small, as it is for many charge particle tracks, the clusters get merged together well. Clusters from showers, as they tend to be very spread out, still need further merging.

The final stage of clustering is shower clustering. This requires there to be a distinction between a cluster object that is shower-like or track-like. To do this, parameters that describe various aspects of a cluster are calculated. The most important features from the cluster parameters are cluster length and spread of the first principle component. More details about track and shower selection are described later in section 6.6.

Once defined as a proto-shower cluster, a 3D charge weighted axis is fit to the cluster's set of space points. The next step is to merge together proto-showers into their respective

showers. The goal for this step is to merge together proto-showers that originate from a primary shower. To do this, a distance of closest approach (DOCA) for each proto-shower cluster axis pair is calculated along with the midpoint from the DOCA line for each pair. Next, the closest distance from the midpoint to both showers are calculated. The angle between the two proto-shower axis is also calculated. A pair of proto-showers that have a DOCA that is less than 5 cm, an angle between 15 and 165 degrees, and both of the conversion lengths are less than 20 cm are merged together. The merging is done for all proto-shower cluster pairs as a final stage of the merging process.

## 6.6 Track and Shower Selection

### 6.6.1 Track Removal

For this analysis track removal is handled in a unique manner. The primary goal is to identify showers coming from a  $\pi^0$ . Therefore, all cuts and optimizations will be tested against shower objects. Being that we simply are trying to identify charged tracks and not particle type, the charge information is not used. The general approach for track removal depends heavily on geometric properties such as length and linearity of the cluster.

### 6.6.2 Single $\pi^0$ Reconstruction

The vast majority (98.8%) of  $\pi^0$ s decay into two photons. The relationship for the particle mass, which was defined in eq 6.1, shows the importance of properly accounting for the energy and angle between the decay photons. To understand a baseline for reconstruction efficiency we have generated a sample of 10,000 single particle  $\pi^0$  events isotropically throughout the detector volume with initial momenta spanning from 0 to 2 GeV.

First we will investigate energy deposited in detector from the decay. An plot of the true kinematic energy of photons from the decay particle is shown in Figure 6.4. It is important to note that both photons need to be reconstructed to form a mass. This means that we are driven to optimize the reconstruction to be robust around showers in the range of many tens of MeV in deposited energy. Photons that convert near the fiducial edge of the detector can escape and deposit only a small amount of energy in the detector. This poses problems

for capturing the total amount of energy of the shower and drives the need for a fiducial cut around the edges.

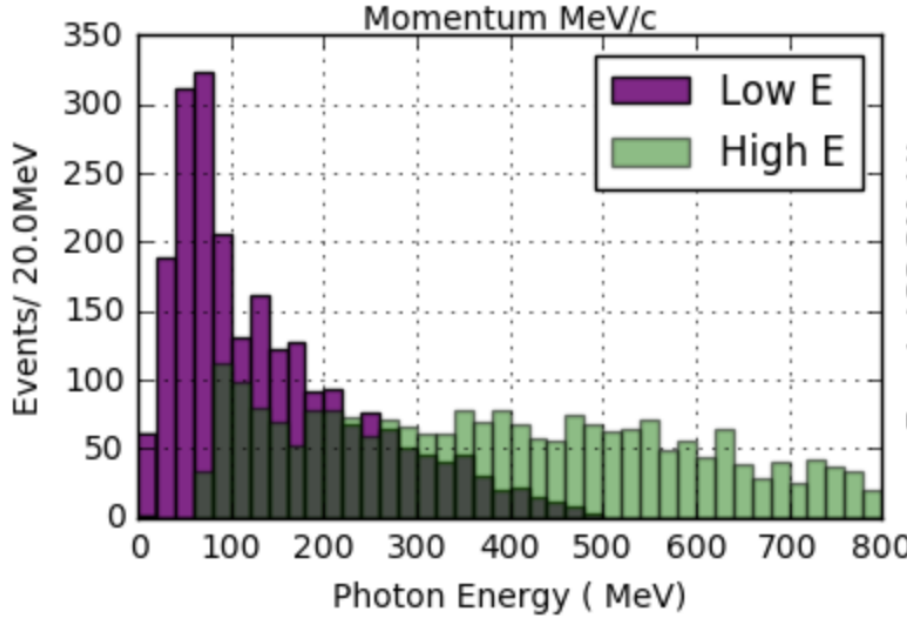
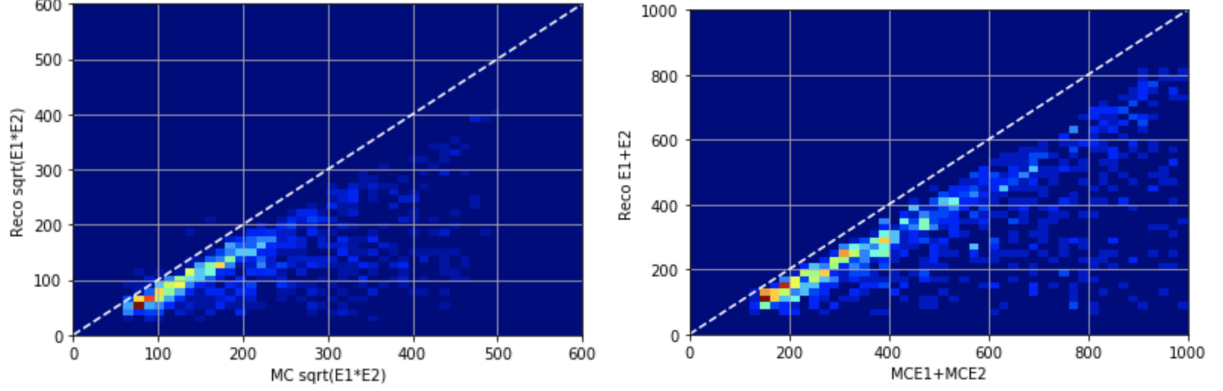


Figure 6.4: This figure shows the photon distribution for  $\pi^0$  decays from a single particle sample of between 0-2 GeV. The higher energy photon is shown above in green along with the corresponding lower energy photon shown in magenta.

To understand the reconstruction accuracy for the energy we are most interested in two metrics. The first is the total collected energy deposited by the two showers. This informs us that we are accounting for most of the energy deposited and handling the fiducial cuts well. The second is the product of the two shower energies. This directly impacts the reconstructed mass resolution and informs us that we are clustering energy between the two showers properly. In figure 6.5 both metrics are plotted for reconstruction against true. Points along the diagonal would represent accurate model predictions. As we will see later in this chapter, the energy product drives the width of the mass resolution.

Next we will investigate the effects of the opening angle between the two photons. The minimum opening angle of the photons is constrained by the momentum boost as the particle decays as shown in equation 6.3. The angular resolution is a very challenging



(a) Scatter plot of reconstructed energy product vs true energy sum  
(b) Scatter plot of reconstructed energy sum vs true energy product

Figure 6.5: Reconstructed energy sum and energy product for shower pairs. Both, the reconstructed energy sum and product is less than the true energy deposited.

problem in LArTPC’s using the traditional 2D projection approach. Fortunately, direct 3D reconstruction improves the angular resolution and allows for a better measurement of shower direction.

$$\sin \frac{1}{2} \theta_{min} = \frac{M}{E_{\pi^0}} \quad (6.3)$$

A plot of the reconstructed vs true opening angle is shown in Figure 6.6. The  $1 - \cos\theta$  term from equation 6.1 is sensitive to tails of the mass distribution.

Next, we apply a final set of selection cuts. First, we require that the distance of closest approach between the two shower axis is less than 5 cm. This is to help ensure that the photons are originating from a common origin. Next, we calculate the opening angle between the two showers and require the angle to be within the range of 20 deg - 160 deg. Also, the photon conversion distance can not be longer than 70 cm for each of the showers. This is done to help identify showers that are correlated from the same decay. Finally we only accept showers that are above 50 MeV in reconstructed energy. Figure 6.7 shows the effect of various parameters as applied to the reconstruction. We find that the deficit in mass peak is mainly due to the energy reconstruction. This is due to the missing

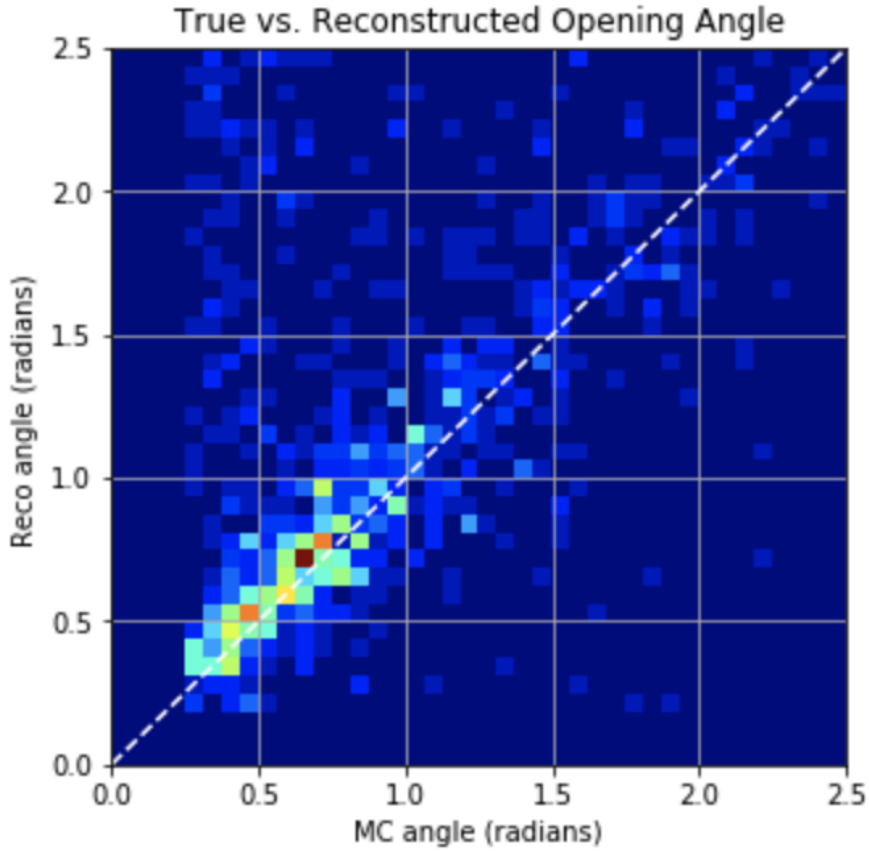


Figure 6.6: This scatter plot shows the reconstructed opening angle vs. true opening angle. We see that the reconstruction does very well with reconstructing this quantity due to the use of wire-cell's 3D approach. When the reconstruction performs badly it tends to identify small opening angles as large ones since we are not using any vertex information.

energy during clustering. For this analysis there is also an additional component of energy missing since we will not be using the initial  $t_0$ -tag. The  $t_0$ -tag is used to identify how far the electrons had to drift to reach the wire plane. Without using  $t_0$ , there is no effective way to correct back for electron drift effects. Thankfully, this effect is can be captured in understanding the distribution of reconstructed mass peak in the Monte Carlo.

Finally, we address the overall efficiency for reconstruction. The average reconstruction efficiency between 0 and 1 GeV/c is 40.1%. The reconstruction efficiency is shown in Figure 6.8. As can be seen there, the efficiency drops at low and high energies. At low

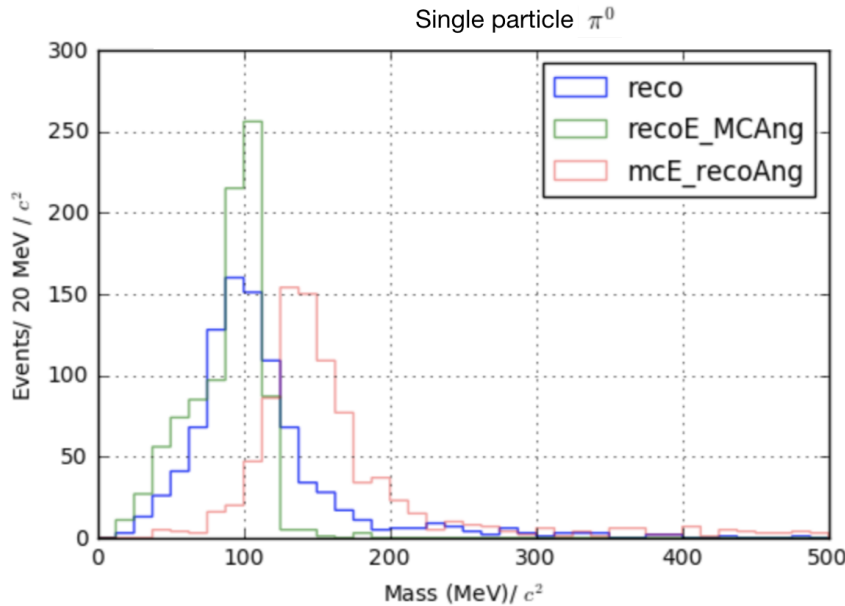


Figure 6.7: The reconstructed mass distribution is shown to highlight effects from reconstruction. First, in blue, the full reconstructed mass is shown. Second, in green, the reconstructed mass is calculated using the true angle. Third, in red, the reconstructed mass is calculated using the true energy.

momentum the  $\pi^0$ s are produced nearly at rest with both showers having similar energies. Most importantly the showers are produced nearly back to back. Without having a well defined vertex, sometime the reconstruction will identify the angle as being close to zero. Being that there is a minimum opening angle cut some of the events are lost from this effect. At high momentum, many of the showers are boosted to small opening angle which we see a similar effect in the loss of efficiency.

## 6.7 Single $\pi^0$ Cosmic Sample

The MicroBooNE cosmics Monte Carlo is generated by CORSIKA (COsmic Ray Simulation for KASCADE) v-7.4003[26]. CORSIKA simulates particles coming from a wide range of interactions initiated by cosmic ray particles in the upper atmosphere. The simulation is robust and accounts for various input parameters such as, longitude and latitude, elevation,

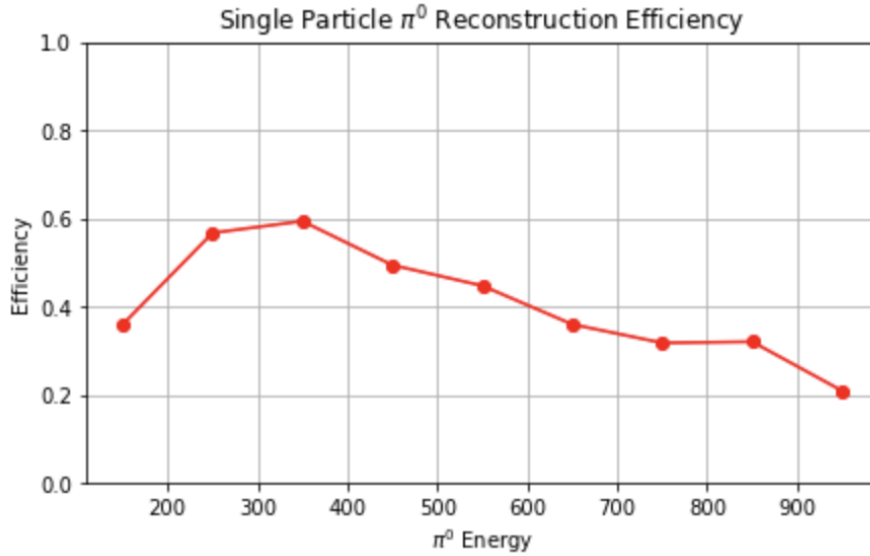


Figure 6.8: The plot shows the  $\pi^0$  reconstruction efficiency for  $\pi^0$ s over a 100-1,000 MeV energy range. The reconstruction efficiency peaks around 350 MeV which conveniently is around the production energy for cosmic  $\pi^0$

and the earth's magnetic field. The particles are simulated over a large region above the detector complex but only particles that travel through the detector cryostat volume are kept. The passage of these particles is simulated by the GEANT4 package. Cosmic rays that do not travel through the cryostat have a low likelihood of producing secondary or tertiary particles that enter the detector TPC volume [27].

In one MicroBooNE drift window (2.3ms) there are on average 6 cosmic muons. The muons do not directly contribute to many EM-showers but sometimes pass through an EM-shower from another particle. For MicroBooNE, the vast majority of muons are through-going and do not lead directly to any method of  $\pi^0$  production.

Various other particles such as, protons, neutrons, and charged pions enter the TPC volume and may produce  $\pi^0$ s. A distribution of  $\pi^0$  production process is shown in Figure 6.9. Nearly half of the  $\pi^0$ s produced in the MicroBooNE TPC are produced through neutron inelastic scattering.

In total, 90,297 CORSIKA truth events were produced to constrain production rates for signal and background. From that, a random sample of 10K events were ran through the

wire-cell imaging reconstruction. Additionally, a signal sample of events which contain a single neutron  $\pi^0$  of  $\approx 1.2\text{K}$  was produced and reconstructed through the wire-cell imaging. The exact rates will be discussed in Chapter 7.

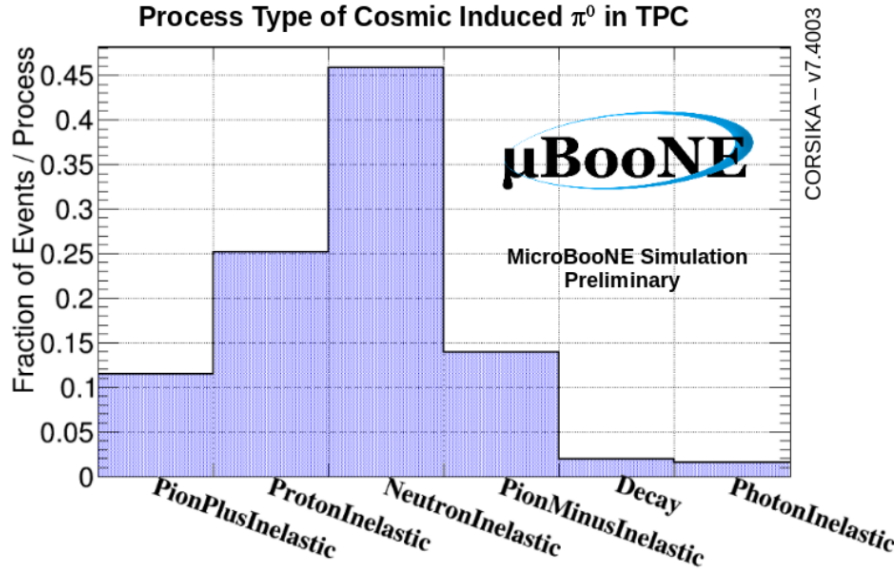


Figure 6.9: Physical process for cosmic  $\pi^0$ s that decay inside the TPC.

MircoBooNE, being a surface detector, has very minimal shielding from cosmic rays. Most of the  $\pi^0$ s coming from protons and charge pions do not make it very far into the detector fiducial volume due to hadronic interactions outside the detector. The building and cryostat easily absorb and re-scatter hadronic particles. This coupled with the argon that is above the TPC provide reduction in charged hadronic particles that make it to the fiducial volume. The neutrons do not interact as much and are slightly more distributed over the TPC fiducial volume. A stacked scatter plot is shown in figure 6.10

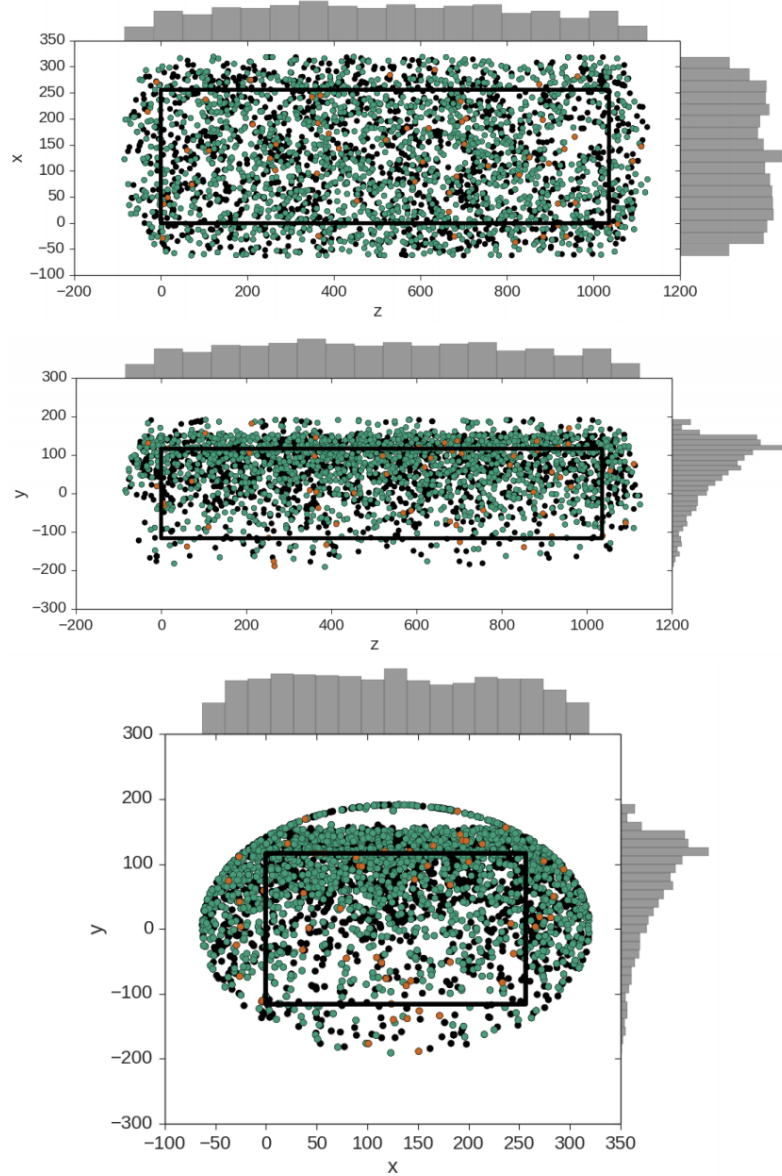


Figure 6.10: These plots show the decay point of actual cosmic  $\pi^0$ s throughout any time in the 4.8 ms window. The green points represent neutron induced  $\pi^0$ s, the orange represent photon induced  $\pi^0$ s, and the black represent a  $\pi^0$  that was produced from a charged particle. In each plot the black box is to represent the entire TPC dimensions not including fiducial cuts. Note that this is a stacked scatter plot with ordering; charged particle (black), photon (orange), neutron (green) from bottom to top.

# Chapter 7

# Results

The goal of this study is primarily two fold. The first goal is to highlight a different technique to reconstruct  $\pi^0$  and EM-showers in an LArTPC. To best showcase this reconstruction technique we will focus on reconstructing  $\pi^0$ s that are induced from a single neutron. In many instances, neutral induced interactions do not have a visible vertex. Reconstructing EM showers from a  $\pi^0$  decay without a vertex poses many challenges for traditional techniques. The Wire-Cell imaging approach allows for a full 3D shower reconstruction without the use of a vertex. The second goal is to measure and compare the cosmic ray neutron induced  $1-\pi^0$  production rate in the MicroBooNE detector. This reconstruction technique is well suited for this type of analysis.

This section will address results from both Monte Carlo and actual MicroBooNE cosmics data. To be clear, we will define our signal to be events that produce 1 and only 1 neutron induce single  $\pi^0$  inside the TPC fiducial volume. For this analysis the fiducial volume is defined from: X [0 cm, 256 cm] , Y[-116 cm, 116 cm], Z[400 cm, 800 cm]. We also restrict our bounds to events that happen in 1 drift window as defined in section 6.7 .

## 7.1 Monte Carlo Simulation

First, a word on simulation constraints. While the wire-cell imaging process provides considerable gains towards extracting high resolution LArTPC reconstruction, it does come with a high computational cost. This was an issue for generating a large sample of Monte

Table 7.1: CORSIKA MC rates

Neutron induced 1 $\pi^0$	1,255
Neutron induced 1 $\pi^0$ outside	13,434
Proton induced 1 $\pi^0$	5,038
Other induced 1 $\pi^0$	9,530
no 1 $\pi^0$ or multi $\pi^0$	61,040

Carlo for Wire-Cell imaging. The process should be able to be distributed, but for this analysis it this process was not yet available. This required us to use an up-sampling technique with the background Monte Carlo sample which is describe in the subsequent paragraphs.

First a enhanced sample of 1,255 signal events were generated from CORSIKA, processed through wire-cell imaging, and reconstructed with the described process in section 6. A background only sample, consisting of 8,720 randomly sampled background events were processed through wire-cell imaging and the reconstruction. This number was then scaled by 0.0139 to obtain an absolute background value relative to the enhanced signal sample. This scaling represents a new total of 90,297 events. One event corresponds to one MicroBooNE readout frame.

From the total sample we find that 1.39% are signal. The remaining background is divided into 5 categories: (1) neutron induced events that are produced outside the fiducial volume, (2) proton induced events that produce 1  $\pi^0$  either inside or outside the fiducial volume, (3) Events that produce 1  $\pi^0$  either inside or outside the fiducial volume not coming from a proton or neutron, (4) Multi  $\pi^0$  produced either inside or outside the fiducial volume, (4) Events that do not contain any  $\pi^0$ . Table 7.1 shows the corresponding counts from the 90,297 CORSIKA sample.

Next, the selection cuts described in chapter 6 are applied to both the signal sample and Monte Carlo. There are a total of 443 events that pass the cuts made in section 6. This corresponds to a signal efficiency of 35.9%. A plot for the reconstructed mass is shown in figure 7.1. The mass peak, which is supposed to be around  $135 \text{ MeV}/c^2$ , is centered around  $100 \text{ MeV}/c^2$  due to the missing energy. This is in agreement with what we expect from the single particle  $\pi^0$  studies from section 6.

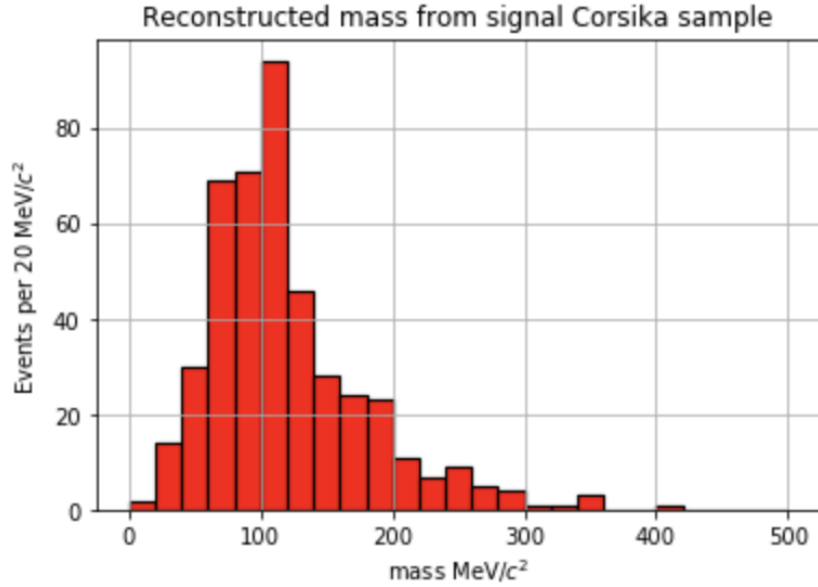


Figure 7.1: Plot of the mass distribution for MC neutron induced signal events.

Then, the same cuts were applied to the background only sample. We find there to be a background rate of 2.3%. Ultimately resulting in a signal:background of 0.21 (approximately 1 : 5.6). A plot of the reconstructed mass distribution for the entire background is shown in figure 7.2

It is important to note that the background distribution will also contain  $\pi^0$  events. The background distribution as described in section 7.1 is plotted in figure 7.2. The distribution should also have some well reconstructed  $\pi^0$ . For this analysis, since we did not require the use of a vertex there is a sizable portion of background that are actual reconstructed  $\pi^0$ . This comes from two primary effects both of which are products of how the reconstruction criteria is defined. The first effect is part of the group coming from events with "No  $\pi^0$ " group. Many of the events are actual  $\pi^0$  particles but reconstructed out side of the fiducial volume. The second effect is in the remaining  $\pi^0$  groups which obviously contains at least one  $\pi^0$ . Being that we remove as many track as possible, many proton and charged pion tracks are removed. In the eyes of the selection process a proton or charged pion induced  $\pi^0$  event has a near identical topology to the signal.

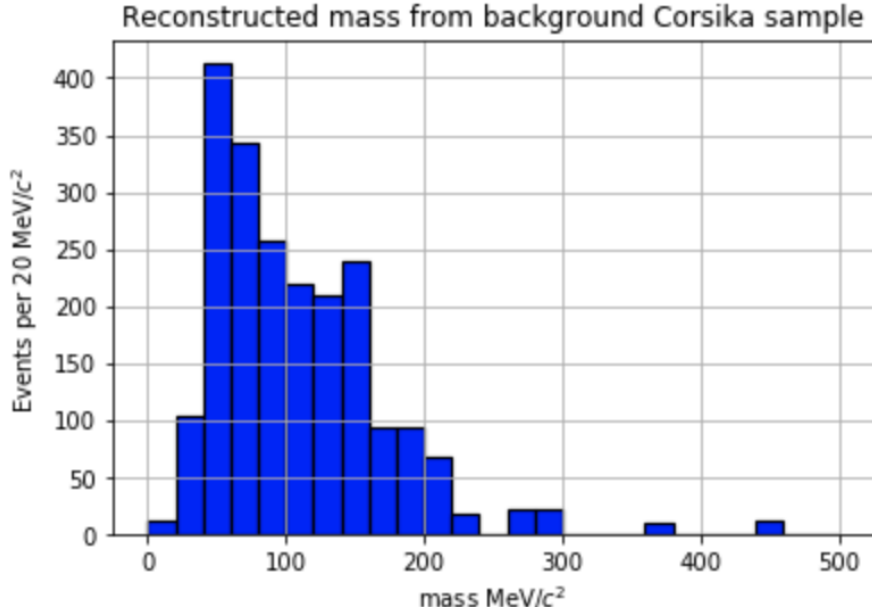


Figure 7.2: Plot of the mass distribution for MC cosmic background events.

## 7.2 Data

The same selection cuts were applied to a dataset of 13,022 off beam cosmic data events that were sampled from the 'MicroBooNE Good Run List'. This is an internal list that MicroBoone generates to define when the detector is in acceptable running mode. This list takes into account various aspects of the detector such as wire stability, argon purity, PMT response, etc. It is important to note that the data sample that is used in this thesis is only from the good run list. Doing this, assumes that any bias in the sample is averaged over for interaction type. The mass distribution is calculated from the given 13,022 sample and there is a clear mass peak from the  $\pi^0$ s that is also centered below the actual  $135 \text{ MeV}/c^2$  mass.

## 7.3 Data-Monte Carlo Comparison

To better understand the data distribution, we first plot an area normalized histogram for Monte Carlo and Data. This is shown in figure 7.3. We see that the shape is indeed similar but not ideal. Given this, the area normalized shape comparison only serves the purpose of

showing that we believe we are reconstructing  $\pi^0$ 's and reasonably handling the background.

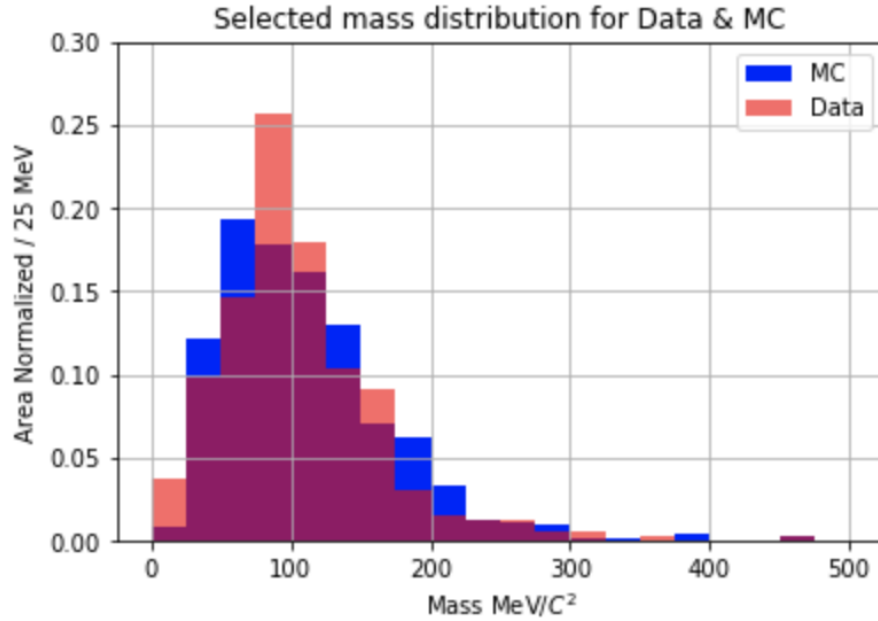


Figure 7.3: Area normalized Data-Monte Carlo mass distributions. The shapes between the data and Monte Carlo distributions provide confidence that we are reconstructing  $\pi^0$ 's in the distribution.

To better compare data and Monte Carlo an absolute rate comparison should be made. This will address how well the Monte Carlo represents the data. The mass distribution is shown in Figure 7.4. Out of the box, CORSIKA slightly over predicts the rate from data producing  $\chi^2/df$  of 1.37. To address this, a  $\chi^2$  minimization can be performed fit the Monte Carlo to the data. Both the signal and background are varied to optimize the fit to data. We will assume a flat 5% systematic error and account for the statistical error of both the Monte Carlo and data. We find that the fit returns a minimum of 0.73  $\chi^2/df$  when the signal is reduced by 72% and the background is also reduced by 84%. The adjusted mass distribution from the fit is shown in Figure 7.5

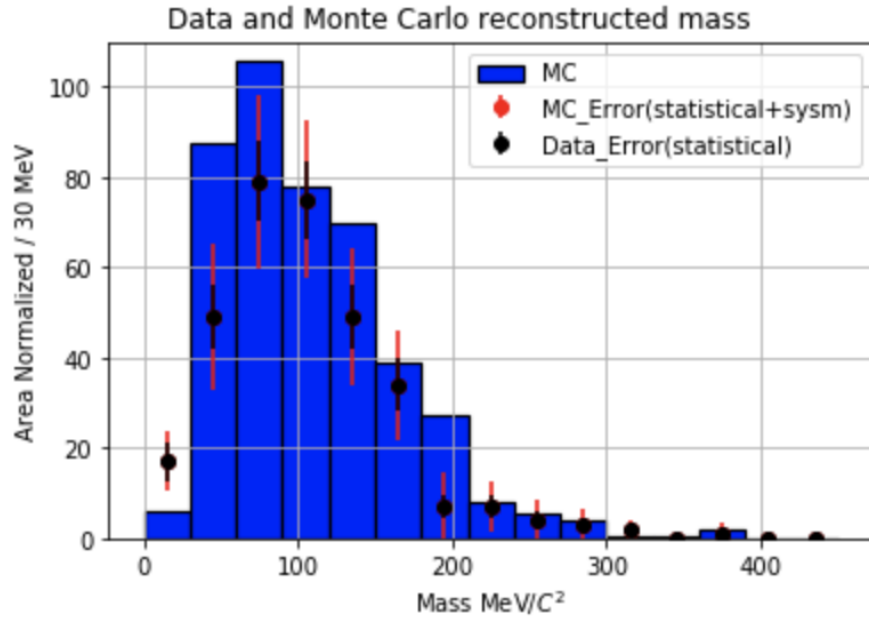


Figure 7.4: This plot shows the mass distribution from data with respect to the unchanged Monte Carlo.

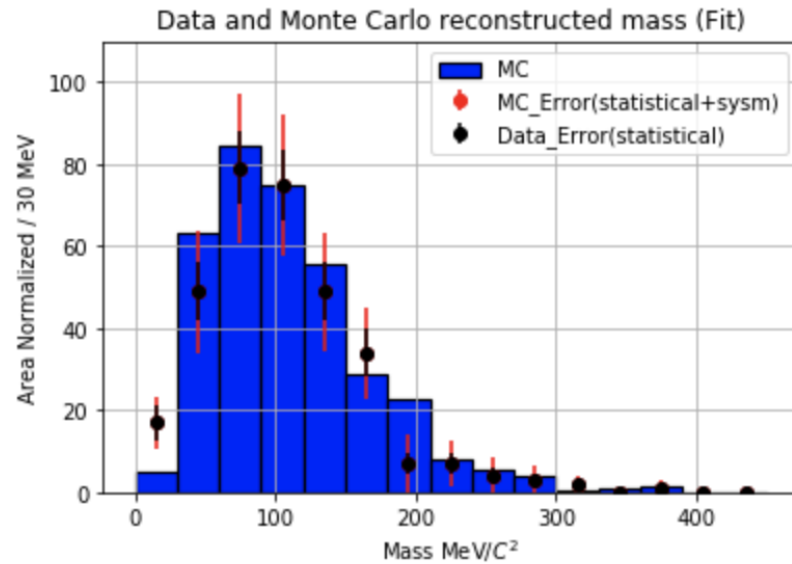


Figure 7.5: This plot shows the mass distribution from data with respect to the fitted Monte Carlo.

# Chapter 8

## Conclusions

### 8.1 Conclusion

The construction of MicroBooNE is an essential step forward for the low energy neutrino physics community. The R&D process provided valuable insights towards future LArTPC detector technology. The MicroBooNE detector was completed in 2015 and has since been collecting valuable data.

This thesis showcases a radically new technique for 3D reconstruction of EM showers. Although wire-cell does require a high amount of computational resources, the improved 3D reconstruction capabilities for EM showers provide justification. Additionally, we are able to reconstruct  $\pi^0$ s without the use of vertex information. We have built an algorithm to identify neutron induced single  $\pi^0$  events. We found that the current CORSIKA Monte Carlo slightly over predicts the rate of neutron induced  $\pi^0$  in the MicroBooNE detector. The data used in this thesis is entirely on cosmic ray data but the extension to a neutral current single  $\pi^0$  interaction is the next logical step.

# Part I

# Appendices

SP0TER is located on Github:

[https://github.com/1grossora>Show\\_Sp0ter](https://github.com/1grossora>Show_Sp0ter)

To obtain a copy of the code you first must have git installed. Next clone the repository to a location of your choice by using the command below.

```
git clone git@github.com:1grossora>Show_Sp0ter.git
```

The requirements are located on the readme page above. Base Requirements:

- Root version: 6.05 or greater
- scipy, numpy, sklearn
- Cython

MC or data from MicroBooNE (not public). A list of important parameters are listed below. The values of these parameters were used for this thesis study but can be varied as the users discretion. More documentation can be found on the github repository page listed above.

Parameter Name	Parameter Value	Location	Parameter Description
charge_thres	500	Utils	Threshold value corresponding to wirecell space point charge
nq_thresh	600	Utils	Max number of charge points in a wirecell blob
zlo	400	Utils	Lower bound z distance
zhi	800	Utils	Upper bound z distance
ylo	116	Utils	Lower bound y distance
yhi	-116	Utils	Upper bound y distance
xlo	-1000	Utils	Lower bound x distance
xhi	1000	Utils	Upper bound x distance
make_json	False	Utils	Produce a json for the BEE display
mincluster	20	Reco	Minimum amount of space points

			needed	67
nn_dist	2	Reco	Minimum distance required for a space point to be merged	
birch_leaf	1000	Reco	Max size of a cluster from birch clustering	
birch_min_cluster	20	Reco	Minimum size of a cluster from birch clustering	
edge_dist	1	Merge	Distance require to merge together hulls from birch clusters	
stitch_mincluster	100	Merge	Minimum number of space points requires to be considered a cluster after stitching	
vari_0	0.9985	Track	Value of the first charge weighted pca of the cluster	
ts_fcl_length	20	Track	Minimum length of hull to designate as a shower	
ts_fcl_minsize	10	Track	Minimum size of the hull to designate as a shower.	
Doca_sweep	10	Shower	Minimum length between two end points of two clusters	
lcmin	25	Shower	Minimum length showers for a final merged shower	
vari_1	0.998	Shower	Value of the second charged weighted PCA of the cluster	
ts_scl_length	25	Shower	Minimum length of shower	
ts_scl_minsize	10	Shower	Minimum volume of the size of showers	
snn_dist	2	Shower	Final showers within this distance are merged.	

# Bibliography

- [1] Henri Becquerel biography. 2014.
- [2] W. Pauli. Open letter to the group of radioactive people at the Gauverein meeting in Tubingen. 1930.
- [3] Y. Fukuda et al. Evidence for oscillation of atmospheric neutrinos. *Phys. Rev. Lett.*, 81:1562–1567, 1998.
- [4] Q. R. Ahmad and others. Measurement of the rate of  $\nu_e + d \rightarrow p + p + e^-$  interactions produced by  ${}^8b$  solar neutrinos at the sudbury neutrino observatory. *Phys. Rev. Lett.*, 87:071301, Jul 2001.
- [5] S. Schael et al. Precision electroweak measurements on the  $Z$  resonance. *Phys. Rept.*, 427:257–454, 2006.
- [6] C. Patrignani et al. Review of Particle Physics. *Chin. Phys.*, C40(10):100001, 2016.
- [7] D. DeCamp and B. Deschizeaux et al. Determination of the number of light neutrino species. *Physics Letters B*, 231(4):519 – 529, 1989.
- [8] C. Rubbia. The Liquid Argon Time Projection Chamber: A New Concept for Neutrino Detectors. 1977.
- [9] S. Amerio and S. Amoruso. et al. Design, construction and tests of the icarus t600 detector. *Nuclear Instruments and Methods in Physics Research Section A: Accelerators, Spectrometers, Detectors and Associated Equipment*, 527(3):329 – 410, 2004.

- [10] C. Anderson et al. The ArgoNeuT Detector in the NuMI Low-Energy beam line at Fermilab. *JINST*, 7:P10019, 2012.
- [11] H. Chen et al. A Proposal for a New Experiment Using the Booster and NuMI Neutrino Beamlines: MicroBooNE.
- [12] A. A. Aguilar-Arevalo et al. Observation of a Significant Excess of Electron-Like Events in the MiniBooNE Short-Baseline Neutrino Experiment. 2018.
- [13] Pip Hamilton. First Measurement of Neutrino Interactions in MicroBooNE. In *18th International Workshop on Neutrino Factories and Future Neutrino Facilities Search (NuFact16) Quy Nhon, Vietnam, August 21-27, 2016*. 2016.
- [14] The microboone technical design report. 2012.
- [15] R. Acciarri et al. Design and Construction of the MicroBooNE Detector. *JINST*, 12(02):P02017, 2017.
- [16] Teppei Katori. The MicroBooNE light collection system. *JINST*, 8:C10011, 2013.
- [17] Costas Andreopoulos, Christopher Barry, Steve Dytman, Hugh Gallagher, Tomasz Golan, Robert Hatcher, Gabriel Perdue, and Julia Yarba. The GENIE Neutrino Monte Carlo Generator: Physics and User Manual. 2015.
- [18] A. A. Aguilar-Arevalo et al. The Neutrino Flux prediction at MiniBooNE. *Phys. Rev.*, D79:072002, 2009.
- [19] A. Aguilar-Arevalo et al. Evidence for neutrino oscillations from the observation of anti-neutrino(electron) appearance in a anti-neutrino(muon) beam. *Phys. Rev.*, D64:112007, 2001.
- [20] A. A. Aguilar-Arevalo et al. The MiniBooNE Detector. *Nucl. Instrum. Meth.*, A599:28–46, 2009.
- [21] A. A. Aguilar-Arevalo et al. Unexplained Excess of Electron-Like Events From a 1-GeV Neutrino Beam. *Phys. Rev. Lett.*, 102:101802, 2009.

- [22] A. Ankowski et al. Energy reconstruction of electromagnetic showers from pi0 decays with the ICARUS T600 Liquid Argon TPC. *Acta Phys. Polon.*, B41:103–125, 2010.
- [23] J. S. Marshall and M. A. Thomson. The Pandora Software Development Kit for Pattern Recognition. *Eur. Phys. J.*, C75(9):439, 2015.
- [24] R. Acciarri et al. Convolutional Neural Networks Applied to Neutrino Events in a Liquid Argon Time Projection Chamber. *JINST*, 12(03):P03011, 2017.
- [25] Xin Qian, Chao Zhang, Brett Viren, and Milind Diwan. Three-dimensional Imaging for Large LArTPCs. *JINST*, 13(05):P05032, 2018.
- [26] D. Heck, G. Schatz, T. Thouw, J. Knapp, and J. N. Capdevielle. CORSIKA: A Monte Carlo code to simulate extensive air showers. 1998.
- [27] S. Agostinelli et al. GEANT4: A Simulation toolkit. *Nucl. Instrum. Meth.*, A506:250–303, 2003.